Chaos, Solitons and Fractals 176 (2023) 114152

Contents lists available at ScienceDirect

Chaos, Solitons and Fractals

journal homepage: www.elsevier.com/locate/chaos

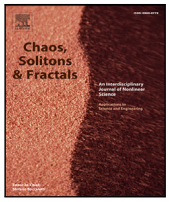

Turing patterns in hyperbolic reaction-transport vegetation models with cross-diffusion

C. Currò [a], G. Grifò [b,*], G. Valenti [b]

[a] Department of Mathematical, Computer, Physical, and Earth Sciences, University of Messina, V.le F. Stagno D'Alcontres 31, 98166 Messina, Italy
[b] Department of Engineering, University of Messina, C.da di Dio, 98166 Messina, Italy

ARTICLE INFO

Keywords:
Hyperbolic reaction-transport model
Extended thermodynamics theory
Linear and weakly nonlinear stability analyses
Cross-diffusion effects
Internal competition rate
Vegetation patterns

ABSTRACT

In this paper, the pattern formation process in arid environments on flat terrains is investigated. In particular, a class of one-dimensional hyperbolic reaction-transport vegetation model with a cross-diffusion term accounting for plant roots' suction in the soil water diffusion feedback is considered. To characterize the emerging Turing patterns, linear stability analysis on the uniform steady states is first addressed. Then, multiple-scale weakly nonlinear analysis is performed to describe the time evolution of the pattern amplitude close to the stability threshold. Finally, to validate analytical predictions, a modified Klausmeier model which takes also into account the internal competition rate is studied. The effects of the inertial times as well as the cross-diffusion and the internal competition rate are illustrated both analytically and numerically.

1. Introduction

In the last decades, climate change and environmental engineering alteration conducted desertification to be one of the main problems that trouble arid and semi-arid ecosystems. Recent works have provided the possibility of the ecosystem undergoing a catastrophic scenario with an abrupt shift or a soft one [1]. A crucial phenomenon that provides additional information about the ecosystem's health is characterized by the formation of vegetation patterns [2]. In particular, they allow us to predict catastrophic scenarios, identify ecological indicators of land degradation, and underline ecosystem resilience. Unfortunately, despite patterns being a characteristic feature of many arid and semi-arid areas, their geographical remoteness together with the long timescale in which they occur, and the absence of laboratory replicates make field studies not trivial at all.

Therefore, theoretical approaches become very useful to analyze the environmental conditions under which such patterns may form and disappear. Thus, a lot of mathematical tools have been provided to build up different models, either deterministic or stochastic, able to reproduce these fascinating structures and to predict the time–space evolution of their dynamics [2–6]. Among them, an appropriate description that may depict this ecological phenomenon, which occurs at the macroscopic level, is based upon continuum theory and the corresponding mathematical models are usually based on parabolic reaction–advection–diffusion systems [7–24].

In this framework, one of the simplest two-compartment models is the Klausmeier one [3], based upon the so-called "water redistribution hypothesis" according to which the local biomass-water positive feedback loop, acting at the micro–scale, is able to give rise to the spatial instabilities at the macro–scale. In detail, the rainwater falls on bare ground characterized by a low infiltration rate and runs off until vegetated areas, marked by a higher infiltration rate. However, the Klausmeier model is not able to describe the complex dynamics occurring in vegetation patterns, so several modified versions have been introduced to account for them by including a diffusion term in the balance equation for water [17,19] and/or an advection term in the balance equation for vegetation [25]. These reaction–advection–diffusion models exhibit a large flexibility over the control of positive feedback mechanisms for the uniform states and admit the formation of subcritical and supercritical bifurcations of the uniform-vegetation state from the bare-soil one. However, most of these generalized versions do not take into account several ecological scenarios, such as the possibility of water to be suctioned by roots plants or the occurrence of an inner competition between plants. Therefore, to fix the first

* Corresponding author.
E-mail addresses: ccurro@unime.it (C. Currò), gabgrifo@unime.it (G. Grifò), gvalenti@unime.it (G. Valenti).

https://doi.org/10.1016/j.chaos.2023.114152
Received 12 June 2023; Received in revised form 28 August 2023; Accepted 5 October 2023

issue, Von Hardenberg et al. [26] introduced a new model that includes the interaction between underground soil moisture and vegetation roots by adding in the water equation a cross-diffusion term, one of the drivers of pattern formation in many biological systems [27–29]. Then, to fix the latter one, the Klausmeier kinetics have been modified by considering a nonlinear infiltration rate that has to mimic the inner competition between biomass [30,31].

Motivated by the experimental evidence of inertia in vegetation dynamics [32–36] as well as to provide a better description of transient regimes, hyperbolic reaction-transport models [37–45] have been introduced in the context of dryland ecology according to the guidelines of Extended Thermodynamics theory [46]. In this framework, the role of inertia in vegetation patterns has been investigated to describe the transitions between spatially homogeneous steady-states and stationary or oscillatory periodic patterned ones. However, to the best of our knowledge, the role of cross-diffusion, as well as the internal competition effects, have never been considered in hyperbolic vegetation reaction-transport models. The aim of this paper is to investigate the role of inertial times in stationary and transient regimes of vegetation bands when both self- and cross-diffusion are taken into account. In detail, we elucidate how the instability threshold of the emerging pattern is affected by the cross-diffusion effects as well as the internal competition rate and how hyperbolicity modifies transient dynamics occurring from a uniform vegetated state to a stationary periodic one.

The paper is organized as follows. In Section 2 a class of 1D hyperbolic reaction-transport models is presented and linear stability analysis is performed to deduce the main features characterizing the emerging Turing-type patterns, i.e. the critical value of the main control parameter as well as the critical wavelength. In Section 3 a weakly nonlinear analysis to describe the amplitude evolution in both supercritical and subcritical regimes as well as to gain more insights into the transient ones is addressed. Then, in Section 4 all the theoretical results are applied to the illustrative example of a modified Klausmeier model [47–49] and numerical investigations are there addressed to validate theoretical results. Finally, concluding remarks are given in the last section.

2. Model and linear stability analysis

In our previous work [39] we proposed a hyperbolic model describing the spatio-temporal evolution of plant biomass $u(x,t)$ and soil–water density $w(x,t)$ in flat environments, which in dimensionless form reads

$$\begin{cases} u_t + J^u_x = f(u,w) \\ w_t + J^w_x = g(u,w) \\ \tau^u J^u_t + u_x = -J^u \\ \tau^w J^w_t + d w_x = -J^w \end{cases} \tag{1}$$

where the subscripts denote the partial derivatives with respect to the indicated variable, J^u and J^w are the dissipative fluxes, τ^u and τ^w are the two constant inertial times, d is the water-to-plant diffusion ratio and the functions $f(u,w)$ and $g(u,w)$ take into account the reactive mechanisms. From the mathematical point of view, the system (1) is strictly hyperbolic and reduces to the corresponding parabolic one in the limit case $\tau^u \to 0$ and $\tau^w \to 0$.

In [39] the system (1) has been investigated to study the inertia effects on vegetation pattern dynamics by choosing kinetic terms characterizing the Klausmeier model [3]. In particular, this study elucidated how the properties exhibited by supercritical and subcritical patterns during the transient regime are affected by the inertial times.

However, ecological observations suggest that vegetation pattern formation is also affected by the suction of water by roots, which are usually described through a cross-diffusion term in Eq. $(1)_2$ [26,31,50–56]. Therefore, to provide a more realistic description of vegetation pattern propagation, the governing system (1) can be replaced in the following vector form

$$\mathbf{U}_t + \mathbf{M}(\mathbf{U})\mathbf{U}_x = \mathbf{N}(\mathbf{U}) \tag{2}$$

where

$$\mathbf{U} = \begin{bmatrix} \mathbf{W} \\ \mathbf{J} \end{bmatrix}, \quad \mathbf{N} = \begin{bmatrix} \mathbf{F} \\ \mathbf{G} \end{bmatrix}, \quad \mathbf{M} = \begin{bmatrix} \mathbf{0} & \mathbf{I} \\ \mathbf{T} & \mathbf{0} \end{bmatrix} \tag{3}$$

with

$$\mathbf{W} = \begin{bmatrix} u \\ w \end{bmatrix}, \quad \mathbf{J} = \begin{bmatrix} J^u \\ J^w \end{bmatrix}, \quad \mathbf{F} = \begin{bmatrix} f(u,w) \\ g(u,w) \end{bmatrix}, \quad \mathbf{T} = \begin{bmatrix} \frac{1}{\tau^u} & 0 \\ -\frac{\beta d}{\tau^w} & \frac{d}{\tau^w} \end{bmatrix}, \quad \mathbf{G} = \begin{bmatrix} -\frac{J^u}{\tau^u} \\ -\frac{J^w}{\tau^w} \end{bmatrix}. \tag{4}$$

Herein $\mathbf{0}$ and $\mathbf{I}$ are the null and the identity matrix whereas β represents the water-uptake ability of plant's roots. From a biological point of view the cross-diffusion coefficient $-\beta d$, denoting the influence of u on w, is negative since water tends to diffuse along the direction of higher concentration of plant biomass. Note that the system (2) belongs to a more general class of hyperbolic reaction-transport model with cross-diffusion for two interacting species [57,58].

Now we briefly recall the main results concerning the linear stability analysis for the hyperbolic model (2) in order to investigate the occurrence of vegetation patterns. To this aim, let $\mathbf{U}^* = (u^*, w^*, 0, 0)$ be a positive steady state, the linearization of the system (2) in the neighborhood of $\mathbf{U}^*$ leads to the dispersion relation, which relates the growth factor ω to the wavenumber k, as follows

$$\omega^4 + A_1\omega^3 + A_2\omega^2 + A_3\omega + A_4 = 0 \tag{5}$$

with

$$
\begin{aligned}
A_1 &= \frac{1}{\tau^u} + \frac{1}{\tau^w} - \left(f_u^* + g_w^*\right), \\
A_2 &= \left(\frac{1}{\tau^u} + \frac{d}{\tau^w}\right) k^2 + b_2, \\
A_3 &= a_3 k^2 + b_3, \\
A_4 &= \frac{1}{\tau^u \tau^w}\left[d k^4 + a_4 k^2 + b_4\right], \\
b_2 &= \frac{1}{\tau^u \tau^w} - \left(f_u^* + g_w^*\right)\left(\frac{1}{\tau^u} + \frac{1}{\tau^w}\right) + f_u^* g_w^* - f_w^* g_u^*, \\
a_3 &= \frac{d+1}{\tau^u \tau^w} - \left(\frac{d f_u^*}{\tau^w} + \frac{g_w^*}{\tau^u}\right) - \frac{\beta d f_w^*}{\tau^w}, \\
b_3 &= \left(\frac{1}{\tau^u} + \frac{1}{\tau^w}\right)\left(f_u^* g_w^* - f_w^* g_u^*\right) - \frac{f_u^* + g_w^*}{\tau^u \tau^w}, \\
a_4 &= -\left(d f_u^* + g_w^* + \beta d f_w^*\right), \\
b_4 &= f_u^* g_w^* - f_w^* g_u^*,
\end{aligned}
\tag{6}
$$

where the asterisk denotes the quantity evaluated at $\mathbf{U}^*$.

In the case of spatially homogeneous perturbations ($k = 0$), Eq. (5) can be factorized as

$$
\left(\omega + \frac{1}{\tau^u}\right)\left(\omega + \frac{1}{\tau^w}\right)\left(\omega^2 - (f_u^* + g_w^*)\omega + \left(f_u^* g_w^* - f_w^* g_u^*\right)\right) = 0 \tag{7}
$$

so that the steady state $\mathbf{U}^*$ is asymptotically linearly stable iff

$$
f_u^* + g_w^* < 0, \qquad f_u^* g_w^* - f_w^* g_u^* > 0. \tag{8}
$$

For what it concerns non-homogeneous perturbations, the linear stability analysis can be carried out by using the Routh–Hurwitz criterion, i.e.

$$
\mathrm{Re}\,\omega < 0 \quad \forall\, \omega \Leftrightarrow A_1 > 0,\ A_3 > 0,\ A_4 > 0,\ A_1 A_2 A_3 > A_3^2 + A_1^2 A_4 \ \forall k. \tag{9}
$$

Therefore, under assumptions (8), A_1 and A_2 are positive for all k and, in turn, the condition $A_3 > 0$ is redundant, so that the Routh–Hurwitz criterion requires

$$
\mathrm{Re}\omega < 0 \quad \forall\, \omega \ \Leftrightarrow\ A_4 > 0, \qquad A_1 A_2 A_3 - A_3^2 - A_1^2 A_4 > 0 \qquad \forall k. \tag{10}
$$

Let us now focus our attention on the occurrence of Turing-like instability as a control parameter is varied. Then, the conditions under which the steady state $\mathbf{U}^*$ is stable to small homogeneous perturbations but it becomes unstable for non-homogeneous ones read [57]

$$
\begin{aligned}
&f_u^* + g_w^* < 0, \quad f_u^* g_w^* - f_w^* g_u^* > 0, \\
&d f_u^* + g_w^* + \beta d f_w^* > 0, \\
&\left(d f_u^* + g_w^* + \beta d f_w^*\right)^2 - 4d\left(f_u^* g_w^* - f_w^* g_u^*\right) > 0, \\
&\xi_2 > 0, \quad \xi_1 + 2\sqrt{\xi_0 \xi_2} > 0
\end{aligned}
\tag{11}
$$

where

$$
\begin{aligned}
\xi_0 &= b_2 b_3 A_1 - b_3^2 - \frac{b_4}{\tau^u \tau^w} A_1^2, \\
\xi_1 &= \left(\frac{1}{\tau^u} + \frac{d}{\tau^w}\right) b_3 A_1 + a_3 b_2 A_1 - 2 a_3 b_3 - \frac{a_4}{\tau^u \tau^w} A_1^2, \\
\xi_2 &= \left(\frac{1}{\tau^u} + \frac{d}{\tau^w}\right) a_3 A_1 - a_3^2 - \frac{d}{\tau^u \tau^w} A_1^2.
\end{aligned}
$$

Consequently, the system (2) undergoes a Turing bifurcation with critical wavenumber

$$
k_c^2 = \sqrt{\frac{f_u^* g_w^* - f_w^* g_u^*}{d}} \tag{12}
$$

for the model parameters such that

$$
4d\left(f_u^* g_w^* - f_w^* g_u^*\right) - \left(d f_u^* + g_w^* + \beta d f_w^*\right)^2 = 0. \tag{13}
$$

Notice that (13) defines implicitly the critical value of a control parameter at which the instability occurs.

As it was observed in [57], the hyperbolic character of the system has no effect on the unstable modes but modifies the Turing regions through the conditions $(11)_4$ which are always satisfied in the parabolic limit. It should be also remarked that, in the absence of cross-diffusion, these conditions give an upper bound on the allowed inertial time $\tau^u < \tau^u_{th} = \frac{1}{f_u^*}$.

3. Weakly nonlinear analysis

As it is well known, the linear stability analysis carried out in the previous section describes the initial phase of small perturbation growth but it does not provide any information on the amplitude of perturbation as well as on transient dynamics. In fact, to predict the pattern amplitude close to the threshold, the nonlinear terms must be included in the analysis. Therefore, let us now perform a multiple-scales weakly nonlinear stability

analysis around the uniform steady state $\mathbf{U}^*$ close to the critical value of a bifurcation parameter, say B. To this aim, we expand the field variables $\mathbf{U}$ as well as the bifurcation parameter B with respect to a positive small parameter $\epsilon \ll 1$ and introduce two different time scales as follows

$$\begin{aligned}
&\mathbf{U} = \mathbf{U}^* + \varepsilon\mathbf{U}_1 + \varepsilon^2\mathbf{U}_2 + \varepsilon^3\mathbf{U}_3 + \varepsilon^4\mathbf{U}_4 + \varepsilon^5\mathbf{U}_5 + O\left(\varepsilon^6\right),\\
&B = B_c + \varepsilon^2 B_2 + \varepsilon^4 B_4 + O\left(\varepsilon^6\right),\\
&\frac{\partial}{\partial t} = \varepsilon^2\frac{\partial}{\partial T_2} + \varepsilon^4\frac{\partial}{\partial T_4} + O\left(\varepsilon^6\right).
\end{aligned} \tag{14}$$

Then, substituting the above expansions (14) into the governing system (2) and collecting terms of the same orders of ε we obtain the following set of linear equations:

$$\begin{aligned}
\frac{\partial \mathbf{U}_1}{\partial x} - K_c^*\mathbf{U}_1 = {} & 0 && \text{at order 1}\\
\frac{\partial \mathbf{U}_2}{\partial x} - K_c^*\mathbf{U}_2 = {} & \tfrac{1}{2}\left(M^{-1}\right)_c^*\left[\left(\mathbf{U}_1\cdot\nabla_U\right)^{(2)}\mathbf{N}\right]_c^* && \text{at order 2}\\
\frac{\partial \mathbf{U}_3}{\partial x} - K_c^*\mathbf{U}_3 = {} & \left(M^{-1}\right)_c^*\left\{B_2\left[\left(\mathbf{U}_1\cdot\nabla_U\right)\frac{\mathrm{d}\mathbf{N}}{\mathrm{d}B}\right]_c^* + \right.\\
& + \left[\left(\mathbf{U}_1\cdot\nabla_U\right)\left(\mathbf{U}_2\cdot\nabla_U\right)\mathbf{N}\right]_c^* +\\
& + \left.\frac{1}{6}\left[\left(\mathbf{U}_1\cdot\nabla_U\right)^{(3)}\mathbf{N}\right]_c^* - \frac{\partial \mathbf{U}_1}{\partial T_2}\right\} && \text{at order 3}\\
\frac{\partial \mathbf{U}_4}{\partial x} - K_c^*\mathbf{U}_4 = {} & \left(M^{-1}\right)_c^*\left\{\tfrac{1}{2}\left[\left(\mathbf{U}_2\cdot\nabla_U\right)^{(2)}\mathbf{N}\right]_c^* + \right.\\
& \left[\left(\mathbf{U}_1\cdot\nabla_U\right)\left(\mathbf{U}_3\cdot\nabla_U\right)\mathbf{N}\right]_c^* +\\
& + \frac{1}{2}\left[\left(\mathbf{U}_1\cdot\nabla_U\right)^{(2)}\left(\mathbf{U}_2\cdot\nabla_U\right)\mathbf{N}\right]_c^* +\\
& + \frac{1}{24}\left[\left(\mathbf{U}_1\cdot\nabla_U\right)^{(4)}\mathbf{N}\right]_c^* + B_2\left[\left(\mathbf{U}_2\cdot\nabla_U\right)\frac{\mathrm{d}\mathbf{N}}{\mathrm{d}B}\right]_c^* +\\
& + \left.\frac{1}{2}B_2\left[\left(\mathbf{U}_1\cdot\nabla_U\right)^{(2)}\frac{\mathrm{d}\mathbf{N}}{\mathrm{d}B}\right]_c^* - \frac{\partial \mathbf{U}_2}{\partial T_2}\right\} && \text{at order 4}\\
\frac{\partial \mathbf{U}_5}{\partial x} - K_c^*\mathbf{U}_5 = {} & \left(M^{-1}\right)_c^*\left\{\left[\left(\mathbf{U}_1\cdot\nabla_U\right)\left(\mathbf{U}_4\cdot\nabla_U\right)\mathbf{N}\right]_c^* + \right.\\
& + \left[\left(\mathbf{U}_2\cdot\nabla_U\right)\left(\mathbf{U}_3\cdot\nabla_U\right)\mathbf{N}\right]_c^* +\\
& + \frac{1}{2}\left[\left(\mathbf{U}_1\cdot\nabla_U\right)^{(2)}\left(\mathbf{U}_3\cdot\nabla_U\right)\mathbf{N}\right]_c^* +\\
& + \frac{1}{2}\left[\left(\mathbf{U}_1\cdot\nabla_U\right)\left(\mathbf{U}_2\cdot\nabla_U\right)^{(2)}\mathbf{N}\right]_c^* +\\
& + \frac{1}{6}\left[\left(\mathbf{U}_1\cdot\nabla_U\right)^{(3)}\left(\mathbf{U}_2\cdot\nabla_U\right)\mathbf{N}\right]_c^* + \frac{1}{120}\left[\left(\mathbf{U}_1\cdot\nabla_U\right)^{(5)}\mathbf{N}\right]_c^* +\\
& + B_2\left[\left(\mathbf{U}_3\cdot\nabla_U\right)\frac{\mathrm{d}\mathbf{N}}{\mathrm{d}B}\right]_c^* + B_2\left[\left(\mathbf{U}_1\cdot\nabla_U\right)\left(\mathbf{U}_2\cdot\nabla_U\right)\frac{\mathrm{d}\mathbf{N}}{\mathrm{d}B}\right]_c^* +\\
& + \frac{1}{6}B_2\left[\left(\mathbf{U}_1\cdot\nabla_U\right)^{(3)}\frac{\mathrm{d}\mathbf{N}}{\mathrm{d}B}\right]_c^* + B_4\left[\left(\mathbf{U}_1\cdot\nabla_U\right)\frac{\mathrm{d}\mathbf{N}}{\mathrm{d}B}\right]_c^* +\\
& + \left.\frac{1}{2}B_2^2\left[\left(\mathbf{U}_1\cdot\nabla_U\right)\frac{\mathrm{d}^2\mathbf{N}}{\mathrm{d}B^2}\right]_c^* - \frac{\partial \mathbf{U}_3}{\partial T_2} - \frac{\partial \mathbf{U}_1}{\partial T_4}\right\} && \text{at order 5}
\end{aligned} \tag{15}$$

where the subscript "c" means that the quantity is evaluated at the critical value of the control parameter B_c and $K_c^* = \left(M^{-1}\nabla\mathbf{N}\right)_c^*$. Moreover, for a generic vector $\mathbf{V}$, the expression $\left(\mathbf{V}\cdot\nabla_U\right)^{(j)}$ denotes the result of applying j times the operator

$$\left(\mathbf{V}\cdot\nabla_U\right) = V_1\frac{\partial}{\partial u} + V_2\frac{\partial}{\partial w} + V_3\frac{\partial}{\partial J^u} + V_4\frac{\partial}{\partial J^w}.$$

Following a similar procedure as the one developed in [57], the solution of the homogeneous linear system $(15)_1$, satisfying zero flux boundary conditions, can be expressed as

$$\mathbf{U}_1 = \Omega\begin{bmatrix}\mathbf{r}\cos\left(k_c x\right)\\ \hat{\mathbf{r}}\sin\left(k_c x\right)\end{bmatrix} \tag{16}$$

where $\Omega\left(T_2, T_4\right)$ is the pattern amplitude. Moreover the vectors $\mathbf{r} = \begin{bmatrix} r_1, & r_2\end{bmatrix}^T$ and $\hat{\mathbf{r}} = \begin{bmatrix} -r_3, & -r_4\end{bmatrix}^T$ satisfy the following systems:

$$\begin{aligned}
&\left(k_c^2\mathbf{D} - \widetilde{\nabla}\mathbf{F}\right)_c^*\mathbf{r} = 0,\\
&\hat{\mathbf{r}} = k_c\mathbf{D}\,\mathbf{r},
\end{aligned} \tag{17}$$

being $\widetilde{\nabla} = \frac{\partial}{\partial \mathbf{W}}$ and $\mathbf{D}$ the non–diagonal diffusion matrix defined by

$$\mathbf{D} = \begin{bmatrix} 1 & 0\\ -\beta d & d\end{bmatrix}. \tag{18}$$

Now, inserting (16) into the nonhomogenous linear system $(15)_2$, the solution at the second perturbative order reads

$$\mathbf{U}_2 = \Omega^2 \begin{bmatrix} \mathbf{U}_{20} + \mathbf{U}_{22}\cos\left(2k_c x\right) \\ \widehat{\mathbf{U}}_{22}\sin\left(2k_c x\right) \end{bmatrix} \tag{19}$$

where

$$\mathbf{U}_{20} = \begin{bmatrix} n_1 \\ n_2 \end{bmatrix}, \quad \mathbf{U}_{22} = \begin{bmatrix} m_1 \\ m_2 \end{bmatrix}, \quad \widehat{\mathbf{U}}_{22} = \begin{bmatrix} m_3 \\ m_4 \end{bmatrix} \tag{20}$$

fulfill the following linear systems

$$\begin{aligned} &\left(\widetilde{\nabla}\mathbf{F}\right)_c^* \mathbf{U}_{20} = -\frac{1}{4}\left(\left(\mathbf{r}\cdot\widetilde{\nabla}\right)^{(2)}\mathbf{F}\right)_c^*, \\ &\left(4k_c^2\mathbf{D} - \widetilde{\nabla}\mathbf{F}\right)_c^* \mathbf{U}_{22} = \frac{1}{2}\left(\left(\mathbf{r}\cdot\widetilde{\nabla}\right)^{(2)}\mathbf{F}\right)_c^*, \\ &\widehat{\mathbf{U}}_{22} = 2k_c\mathbf{D}\,\mathbf{U}_{22}. \end{aligned} \tag{21}$$

Then, taking into account (16)–(19), the elimination of secular terms at the third perturbative order $(15)_3$ leads to the following Stuart-Landau equation for the pattern amplitude Ω

$$\frac{\mathrm{d}\Omega}{\mathrm{d}T_2} = \sigma\Omega - L\Omega^3 \tag{22}$$

where the growth rate σ and Landau coefficient L are given by

$$\begin{aligned} \sigma &= \frac{B_2\left[r_1\left(\beta d t_1 + t_2\right) - d r_2 t_1\right]}{r_1\left\{r_2 + d\left(r_2 - \beta r_1\right)\left[k_c^2\left(\tau^u - \tau^w\right) - 1\right]\right\}}, \\ L &= \frac{d\left(r_2 - \beta d r_1\right)\left(p_1 + 8q_1 + 4s_1\right) - r_1\left(p_2 + 8q_2 + 4s_2\right)}{8r_1\left\{r_2 + d\left(r_2 - \beta r_1\right)\left[k_c^2\left(\tau^u - \tau^w\right) - 1\right]\right\}} \end{aligned} \tag{23}$$

with

$$\begin{aligned} \mathbf{p} &= \begin{bmatrix} p_1 \\ p_2 \end{bmatrix} = \left(\left(\mathbf{r}\cdot\widetilde{\nabla}\right)^{(3)}\mathbf{F}\right)_c^*, \\ \mathbf{q} &= \begin{bmatrix} q_1 \\ q_2 \end{bmatrix} = \left(\mathbf{r}\cdot\widetilde{\nabla}\right)\left(\left(\mathbf{U}_{20}\cdot\widetilde{\nabla}\right)\mathbf{F}\right)_c^*, \\ \mathbf{s} &= \begin{bmatrix} s_1 \\ s_2 \end{bmatrix} = \left(\mathbf{r}\cdot\widetilde{\nabla}\right)\left(\left(\mathbf{U}_{22}\cdot\widetilde{\nabla}\right)\mathbf{F}\right)_c^*, \\ \mathbf{t} &= \begin{bmatrix} t_1 \\ t_2 \end{bmatrix} = \left(\left(\mathbf{r}\cdot\widetilde{\nabla}\right)\frac{d\mathbf{F}}{dB}\right)_c^*. \end{aligned} \tag{24}$$

It should be noticed that, in the Turing region, the growth rate coefficient σ is always positive and the sign of the Landau coefficient L, which depends on the model parameters, describes two different qualitative behaviors. In particular, the supercritical regime is related to $L > 0$ whereas the subcritical one to $L < 0$.

Let us now focus on the supercritical dynamics characterized by the positiveness of the Landau coefficient L. In this case, the Stuart-Landau Eq. (22) admits the nontrivial stable equilibrium

$$\Omega_\infty^{(\mathrm{super})} = \sqrt{\frac{\sigma}{L}} \tag{25}$$

corresponding to the asymptotic value of the pattern amplitude Ω. Moreover, by integrating (22), the temporal evolution of the supercritical pattern amplitude is ruled by

$$\Omega\left(T_2\right) = \frac{\Omega_0 \exp\left(\sigma T_2\right)}{\sqrt{1 + \frac{\Omega_0^2}{\Omega_\infty^2}\left[\exp\left(2\sigma T_2\right) - 1\right]}} \tag{26}$$

where Ω_0 is the initial amplitude perturbation. Notice that, as it is expected, the stationary amplitude $\Omega_\infty^{(\mathrm{super})}$ does not depend on the inertial times, whereas the transient dynamics are affected by the hyperbolic structure of the system through the parameter σ. However, taking into account $(23)_1$, it is easy to ascertain that the hyperbolic structure of the model does not affect the pattern dynamics if the inertial times offset each other, i.e. when $\tau^u = \tau^w$.

Therefore, the stationary solution of the governing system (2) at the second order approximation, provided by the weakly nonlinear analysis, is given by

$$\mathbf{U}(x) = \mathbf{U}^* + \varepsilon\sqrt{\frac{\sigma}{L}}\begin{bmatrix} \mathbf{r}\cos\left(k_c x\right) \\ \widehat{\mathbf{r}}\sin\left(k_c x\right) \end{bmatrix} + \varepsilon^2\frac{\sigma}{L}\begin{bmatrix} \mathbf{U}_{20} + \mathbf{U}_{22}\cos\left(2k_c x\right) \\ \widehat{\mathbf{U}}_{22}\sin\left(2k_c x\right) \end{bmatrix} + O(\varepsilon^3). \tag{27}$$

On the contrary, in the subcritical regime ($L < 0$) the cubic Stuart-Landau Eq. (22) does not admit any stable equilibrium so that we have to push the weakly nonlinear analysis up to the fifth order. Then, the pattern amplitude Ω satisfies the quintic Stuart–Landau equation

$$\frac{\mathrm{d}\Omega}{\mathrm{d}T} = \overline{\sigma}\,\Omega - \overline{L}\,\Omega^3 + \overline{R}\,\Omega^5 \tag{28}$$

where

$$\begin{aligned} &\frac{\mathrm{d}}{\mathrm{d}T} = \frac{\partial}{\partial T_2} + \varepsilon^2 \frac{\partial}{\partial T_4}, \\ &\overline{\sigma} = \sigma + \varepsilon^2 \widetilde{\sigma}, \qquad \overline{L} = L + \varepsilon^2 \widetilde{L}, \qquad \overline{R} = \varepsilon^2 \widetilde{R}. \end{aligned} \tag{29}$$

The expressions of the new corrections $\widetilde{\sigma}$, $\widetilde{L}$ and $\widetilde{R}$, arising when higher order terms are considered, will be provided in the next section for the illustrative example. Moreover, since $\sigma > 0$ and $L < 0$, there exists $\varepsilon \ll 1$ such that $\overline{\sigma} > 0$, $\overline{L} < 0$ and in turn, when $\overline{R} < 0$, there exists one non trivial stable stationary amplitude given by:

$$\Omega_{\infty}^{(\mathrm{sub})} = \sqrt{\frac{\overline{L} - \sqrt{\overline{L}^2 - 4\overline{R}\overline{\sigma}}}{2\overline{R}}}. \tag{30}$$

Then, the integration of the quintic Stuart–Landau Eq. (28) implicitly defines the time evolution of the pattern amplitude $\Omega(T)$ as follows

$$T = \frac{1}{4\overline{\sigma}\chi}\left[4\chi \ln\left(\frac{\Omega}{\Omega_0}\right) + \left(\overline{L} - \chi\right)\ln\left(\frac{2\overline{R}\Omega^2 - \overline{L} - \chi}{2\overline{R}\Omega_0^2 - \overline{L} - \chi}\right) - \left(\overline{L} + \chi\right)\ln\left(\frac{2\overline{R}\Omega^2 - \overline{L} + \chi}{2\overline{R}\Omega_0^2 - \overline{L} + \chi}\right)\right] \tag{31}$$

where $\chi = \left(\overline{L}^2 - 4\overline{R}\overline{\sigma}\right)^{1/2}$.

Finally, according to $(14)_1$ and under the assumption $\overline{R} < 0$, the stationary solution of the governing system (2) at the fourth order approximation is given by

$$\begin{aligned} \mathbf{U}(x) = \mathbf{U}^* &+ \varepsilon\Omega_{\infty}\begin{bmatrix} \mathbf{r}\cos\left(k_c\, x\right) \\ \hat{\mathbf{r}}\sin\left(k_c\, x\right) \end{bmatrix} + \varepsilon^2\Omega_{\infty}^2\begin{bmatrix} \mathbf{U}_{20} + \mathbf{U}_{22}\cos\left(2k_c\, x\right) \\ \hat{\mathbf{U}}_{22}\sin\left(2k_c\, x\right) \end{bmatrix} + \\ &+\varepsilon^3\Omega_{\infty}\begin{bmatrix} \left(\mathbf{U}_{31} + \Omega_{\infty}^2\mathbf{U}_{32}\right)\cos\left(k_c\, x\right) + \Omega_{\infty}^2\mathbf{U}_{33}\cos\left(3k_c\, x\right) \\ \left(\hat{\mathbf{U}}_{31} + \Omega_{\infty}^2\hat{\mathbf{U}}_{32}\right)\sin\left(k_c\, x\right) + \Omega_{\infty}^2\hat{\mathbf{U}}_{33}\sin\left(3k_c\, x\right) \end{bmatrix} + \\ &+\varepsilon^4\Omega_{\infty}^2\begin{bmatrix} \mathbf{U}_{40} + \Omega_{\infty}^2\mathbf{U}_{41} + \left(\mathbf{U}_{42} + \Omega_{\infty}^2\mathbf{U}_{43}\right)\cos\left(2k_c\, x\right) + \Omega_{\infty}^2\mathbf{U}_{44}\cos\left(4k_c\, x\right) \\ \left(\hat{\mathbf{U}}_{42} + \Omega_{\infty}^2\hat{\mathbf{U}}_{43}\right)\sin\left(2k_c\, x\right) + \Omega_{\infty}^2\hat{\mathbf{U}}_{44}\sin\left(4k_c\, x\right) \end{bmatrix} + O(\varepsilon^5) \end{aligned} \tag{32}$$

where we omitted the superscript "(sub)" to make (32) more readable. Details on the derivation of quintic Stuart–Landau Eq. (28) are given in Appendix.

4. Illustrative example: a modified Klausmeier model

In this section, we apply the results previously obtained to a modified Klausmeier model to investigate the effects of internal competition reaction between biomass on the vegetation spatial pattern formation. In fact, in arid or semi-arid regions, the lack of water resources leads to plant competition for survival. Therefore, the kinetic terms, which take into account the fact that inner competition increases in more vegetated areas, can be expressed as follows [30,31]

$$\begin{aligned} f(u,w) &= \frac{w\,u^2}{1+\alpha u^2} - B\,u, \\ g(u,w) &= A - w - \frac{w\,u^2}{1+\alpha u^2}. \end{aligned} \tag{33}$$

In (33) the adimensional parameters B and A represent the plant loss and rainfall rate which, as suggested by previous investigations, belong to the ranges $B \in (0,2)$ and $A \in (0,3)$ [3,59], whereas the parameter α takes into account the inner competition between biomass. Notice that, for $\alpha = 0$ we recover the kinetics terms characterizing the Klausmeier model.

The spatially homogeneous equilibrium states $\mathbf{U}^* \equiv (u^*, w^*, \boldsymbol{J}^{u^*}, \boldsymbol{J}^{w^*})$ admitted by (2), (33) depend upon the value of the rainfall A and the plant loss B, namely

$$\begin{aligned} &A < A_{ex} \quad \Rightarrow \quad \text{desert state} \qquad \mathbf{U}_D^* \equiv (0, A, 0, 0)\,, \\ &A > A_{ex} \quad \Rightarrow \quad \text{three equilibria} \quad \mathbf{U}_D^*,\, \mathbf{U}_{S,L}^* = \left(u_{S,L}, \frac{B}{u_{S,L}}(1+\alpha u_{S,L}^2), 0, 0\right), \end{aligned} \tag{34}$$

with

$$\begin{aligned} &A_{ex} = 2B\sqrt{1+\alpha}, \\ &0 < u_L = \frac{A - \sqrt{A^2 - 4B^2(\alpha+1)}}{2B(\alpha+1)} < \frac{1}{\sqrt{1+\alpha}} < u_S = \frac{A + \sqrt{A^2 - 4B^2(\alpha+1)}}{2B(\alpha+1)}. \end{aligned} \tag{35}$$

In the particular case when $A = A_{ex}$ the system admits, in addition to the desert state, only one steady-state being $\mathbf{U}_S^* = \mathbf{U}_L^* = \left(\frac{1}{\sqrt{1+\alpha}}, \frac{B(1+2\alpha)}{\sqrt{1+\alpha}}, 0, 0\right)$.

According to the linear stability analysis carried out in previous section, the dispersion relation (5) is obtained with

$$
\begin{aligned}
A_1 &= \frac{(\tau^u+\tau^w)\left(1+\alpha u_S^2\right)-\tau^u\tau^w\left[B-1-(1+B\alpha+\alpha)u_S^2\right]}{\tau^u\tau^w\left(1+\alpha u_S^2\right)},\\
A_2 &= \frac{(d\tau^u+\tau^w)\left(1+\alpha u_S^2\right)k^2+1+\alpha u_S^2-(\tau^u+\tau^w)\left[B-1-(1+B\alpha+\alpha)u_S^2\right]}{\tau^u\tau^w\left(1+\alpha u_S^2\right)},\\
A_3 &= \frac{\left\{(d+1)\left(1+\alpha u_S^2\right)-dB\tau^u+\tau^w+\left[\tau^u+\alpha\tau^w+d\tau^u(\alpha B-\beta)\right]u_S^2\right\}k^2}{\tau^u\tau^w\left(1+\alpha u_S^2\right)}+\\
&\quad+\frac{\left\{1-B(1+\tau^u+\tau^w)+\left[1+\alpha+B(\tau^u+\tau^w)+B\alpha(1+\tau^u+\tau^w)\right]u_S^2\right\}}{\tau^u\tau^w\left(1+\alpha u_S^2\right)},\\
A_4 &= \frac{d\left(1+\alpha u_S^2\right)k^4-\left[dB-1-(1+\alpha+dB\alpha-d\beta)u_S^2\right]k^2+B\left[(1+\alpha)u_S^2-1\right]}{\tau^u\tau^w\left(1+\alpha u_S^2\right)}.
\end{aligned}
\tag{36}
$$

Then, taking into account

$$
\begin{aligned}
&f_u(\mathbf{U}_D^*)=-B, \qquad f_w(\mathbf{U}_D^*)=0, \qquad g_u(\mathbf{U}_D^*)=0, \qquad g_w(\mathbf{U}_D^*)=-1,\\
&f_u(\mathbf{U}_{S,L}^*)=\frac{B\left(1-\alpha u_{S,L}^2\right)}{1+\alpha u_{S,L}^2}, \quad f_w(\mathbf{U}_{S,L}^*)=\frac{u_{S,L}^2}{1+\alpha u_{S,L}^2}, \quad g_u(\mathbf{U}_{S,L}^*)=-\frac{2B}{1+\alpha u_{S,L}^2}, \quad g_w(\mathbf{U}_{S,L}^*)=-\frac{1+(1+\alpha)u_{S,L}^2}{1+\alpha u_{S,L}^2},
\end{aligned}
\tag{37}
$$

it can be easily checked that the desert state $\mathbf{U}_D^*$ is always stable, the vegetated state $\mathbf{U}_L^*$ is always unstable whereas the stability of the steady state $\mathbf{U}_S^*$ depends on the values of A and B. Consequently, patterned solutions may be observed as a destabilization of the homogeneously vegetated state $\mathbf{U}_S^*$.

Therefore the necessary conditions (11) for diffusion-driven instabilities yielding Turing–like patterns specialize to

$$
\begin{cases}
B-1-(1+B\alpha+\alpha)u_S^2<0\\
B\left[u_S^2(1+\alpha)-1\right]>0\\
dB-1-(1+\alpha+dB\alpha-d\beta)u_S^2>0\\
\left[dB-1-(1+dB\alpha+\alpha-d\beta)u_S^2\right]^2-4dB\left(1+\alpha u_S^2\right)\left[u_S^2(1+\alpha)-1\right]>0\\
\xi_2>0\\
\xi_1+2\sqrt{\xi_0\xi_2}>0
\end{cases}
\tag{38}
$$

where

$$
\begin{aligned}
\xi_0 &= \frac{(\tau^u+\tau^w)\left[1-B+(1+B\alpha+\alpha)u_S^2\right]\left\{B(\tau^u)^2\left[(1+\alpha)u_S^2-1\right]-\tau^u\left[B-1-(1+B\alpha+\alpha)u_S^2\right]+1+\alpha u_S^2\right\}}{(\tau^u\tau^w)^3\left(1+\alpha u_S^2\right)^3}\times\\
&\quad\times\left\{B(\tau^w)^2\left[(1+\alpha)u_S^2-1\right]-\tau^w\left[B-1-(1+B\alpha+\alpha)u_S^2\right]+1+\alpha u_S^2\right\},\\
\xi_1 &= \frac{c_1 d u_S^2\beta+c_2\left[1+\alpha u_S^2-\tau^u B\left(1-\alpha u_S^2\right)\right]+c_3\left[1+\alpha u_S^2+\tau^w\left(1+(1+\alpha)u_S^2\right)\right]^2+(d-1)(\tau^u+\tau^w)\left[\tau^u B\left(1-\alpha u_S^2\right)+\tau^w\left(1+(1+\alpha)u_S^2\right)\right]}{(\tau^u\tau^w)^3\left(1+\alpha u_S^2\right)^3},\\
\xi_2 &= -\frac{\left\{d\beta(\tau^u)^2u_S^2+(d\tau^u-\tau^w)\left[\tau^u B-1-\alpha u_S^2(1+\tau^u B)\right]\right\}\left[d\beta\tau^u\tau^w u_S^2+(d\tau^u-\tau^w)\left(\tau^w+\tau^w(1+\alpha)u_S^2+1+\alpha u_S^2\right)\right]}{(\tau^u\tau^w)^3\left(1+\alpha u_S^2\right)^2},
\end{aligned}
\tag{39}
$$

with

$$
\begin{aligned}
c_1 &= \tau^w(\tau^u+\tau^w)\left(1+\alpha u_S^2\right)\left\{1+\alpha u_S^2+B(\tau^u)^2\left[u_S^2(1+\alpha)-1\right]\right\}-(\tau^u)^3\tau^w\left[B-1-(1+B\alpha+\alpha)u_S^2\right]^2+\\
&\quad+\tau^u\left[B-1-(1+B\alpha+\alpha)u_S^2\right]\left\{\left(1+\alpha u_S^2\right)\left[(\tau^u)^2-\tau^u\tau^w-(\tau^w)^2\right]+(\tau^u\tau^w)^2B\left[u_S^2(1+\alpha)-1\right]\right\},\\
c_2 &= \left\{\tau^w\left[\tau^w B\left(u_S^2(1+\alpha)-1\right)-B+1+(1+B\alpha+\alpha)u_S^2\right]\right\}\left\{(\tau^u+\tau^w)\left(1+\alpha u_S^2\right)+\right.\\
&\quad\left.-d(\tau^u)^2\left[B-1-(1+B\alpha+\alpha)u_S^2\right]\right\}+d\left(1+\alpha u_S^2\right)\left\{(\tau^u+\tau^w)\left(1+\alpha u_S^2\right)-(\tau^u)^2\left[B-1-(1+B\alpha+\alpha)u_S^2\right]\right\},\\
c_3 &= \left\{\tau^u\left[\tau^u B\left(u_S^2(1+\alpha)-1\right)-B+1+(1+B\alpha+\alpha)u_S^2\right]\right\}\left\{d(\tau^u+\tau^w)\left(1+\alpha u_S^2\right)+\right.\\
&\quad\left.-d(\tau^w)^2\left[B-1-(1+B\alpha+\alpha)u_S^2\right]\right\}+\left(1+\alpha u_S^2\right)\left\{(\tau^u+\tau^w)\left(1+\alpha u_S^2\right)-(\tau^w)^2\left[B-1-(1+B\alpha+\alpha)u_S^2\right]\right\}.
\end{aligned}
\tag{40}
$$

Furthermore, choosing the plant loss B as the bifurcation parameter, the stationary pattern solution occurs at the critical values (12)–(13) which reduce to:

$$
\begin{aligned}
k_c^2 &= \sqrt{\frac{B_c\left[(1+\alpha)u_{S_c}^2-1\right]}{d\left(1+\alpha u_{S_c}^2\right)}}\\
4dB_c\left(1+\alpha u_{S_c}^2\right)\left[(1+\alpha)u_{S_c}^2-1\right]&-\left[dB_c-1-\left(1+dB_c\alpha+\alpha-d\beta\right)u_{S_c}^2\right]^2=0
\end{aligned}
\tag{41}
$$

with $u_{S_c}=\frac{A+\sqrt{A^2-4B_c^2(\alpha+1)}}{2B_c(\alpha+1)}$.

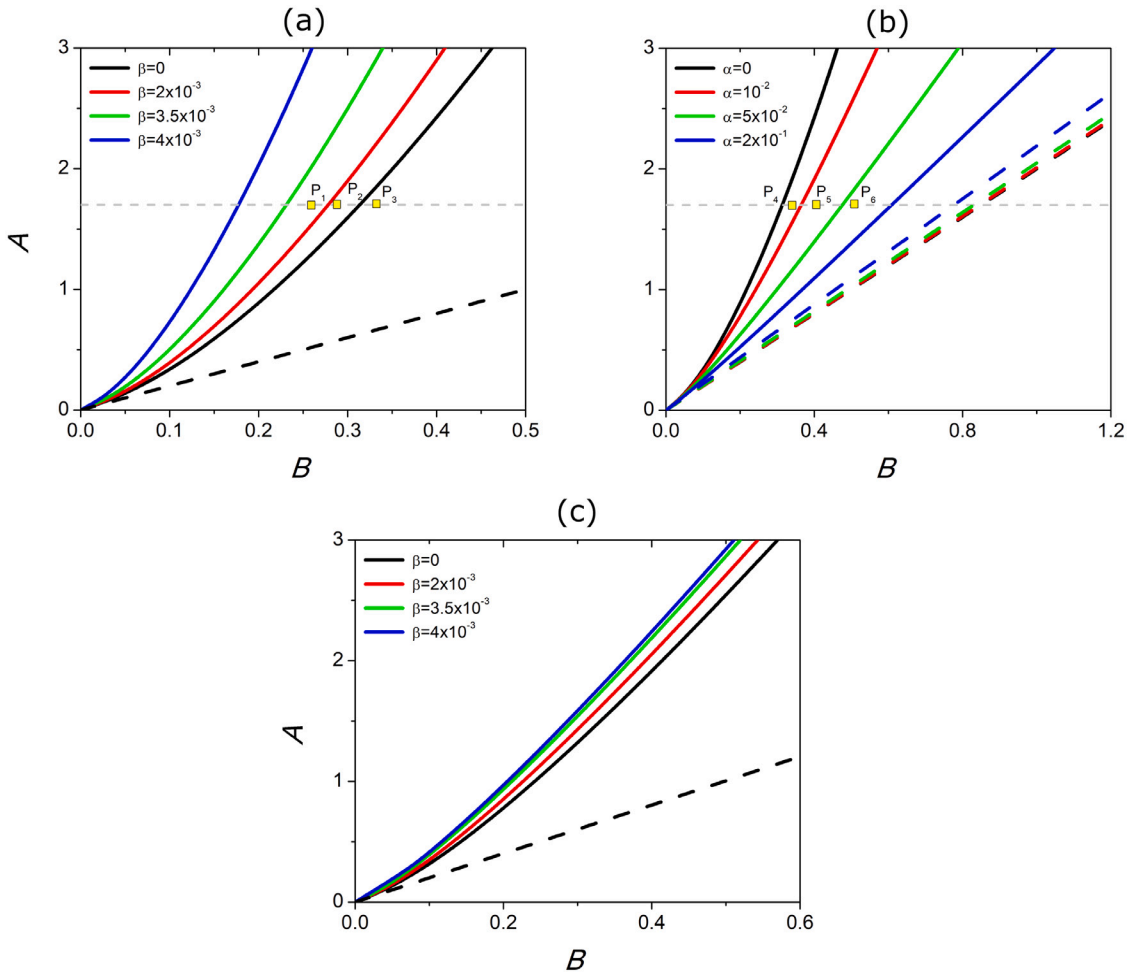

Fig. 1. Bifurcation diagram in the (B, A)-plane for different values of β (a, c) and α (b). The Turing loci are denoted by solid lines, whereas the dashed ones define the loci $A = A_{ex}$. Fixed parameters: $d = 500$, $\alpha = 0$ in (a), $\beta = 0$ in (b) and $\alpha = 10^{-2}$ in (c). Yellow squares represent the configurations $P_1 = (0.25, 1.7)$, $P_2 = (0.30, 1.7)$, $P_3 = (0.32, 1.7)$, $P_4 = (0.34, 1.7)$, $P_5 = (0.40, 1.7)$ and $P_6 = (0.50, 1.7)$.

Let us now address numerical investigations to validate these analytical results and gain some insight into the combined role of the inertial times τ^u and τ^w, the cross-diffusion term β and the internal competition rate α on the vegetated patterns dynamics.

To this aim, we build up the bifurcation diagram in the (B, A)-plane in Fig. 1 for different values of β [panels (a, c)] and α [panel (b)] by fixing $d = 500$. In detail, in panel (a) we fix $\alpha = 0$ by focusing on the role of the cross-diffusion term β, in panel (b) we fix $\beta = 0$ to underline the effects of the internal competition rate α whereas in panel (c) we fix $\alpha = 10^{-2}$ to investigate the combined role of the above parameters. In these figures, the solid curve represents the bifurcation locus $(41)_2$ whereas the dashed line denotes the existence condition $A = A_{ex}$ $(35)_1$. The curves separate the (B, A) parametric plane into three different regions: the one below the line $A = A_{ex}$ where the only desert state $\mathbf{U}_D^*$ exists and it is stable, the one between dashed and solid line where vegetated patterns may be observed since $\mathbf{U}_S^*$ is destabilized by nonhomogeneous perturbations and, finally, the one lying above such bifurcation locus where the bistability between $\mathbf{U}_D^*$ and $\mathbf{U}_S^*$ is observed. From a direct inspection we can deduce that the cross-diffusion term favors the destabilization of the spatially-homogeneous vegetated states $\mathbf{U}_S^*$ as the instability region enlarges itself when β is increased [panel (a)]. Ecologically this means that, when roots have a strong ability of absorbing the soil water, the growth of surrounding vegetation is inhibited and this induces a stripe distribution. On the contrary, when β is neglected, the increase of the internal competition rate leads to a reduction of the Turing region by following a double effect: (i) the instability threshold $(41)_2$ occurs for bigger values of plant loss B and (ii) the existence condition $(35)_1$ shifts up [see panel (b)]. From the ecological viewpoint, these phenomena are strictly correlated to the fact that, when the internal competition increases, vegetation plants have less availability of environmental resources, so the desert state is favored. Finally, when both β and α are taken into account, the effects can offset each other [see panel (c)].

Then, to characterize the wavelength dependence on the above parameters, we analyze the range of unstable wavenumbers and the critical one in Fig. 2 by varying β and α. As it is known, if a non-homogeneous perturbation is applied close to the onset of instability to $\mathbf{U}_S^*$, the system converges to a patterned configuration whose wavenumber is near to the mode exhibiting the largest growth rate. On the contrary, if we move away from the critical threshold B_c, a range of unstable wavenumbers arises and the competition of excitable modes occurs. In particular, at the onset of instability B_c, this range degenerates into the single value k_c [see the turning points in panels (a, c)]. To better address this point, Fig. 2(a,c) depict the variations in the (B, k)-plane of the root of the characteristic polynomial (5), (36) associated to the most unstable mode for different values of β [panel (a)] and α [panel (c)]. Results here achieved confirmed the prediction shown in Fig. 1. Indeed, when α is neglected it can be observed that the increase of cross-diffusion strength leads to an enlargement of the range of the excitable modes. On the contrary, if the role of β is not taken into account, the internal competition effects bring a reduction of the above-mentioned region. Details regarding the value of

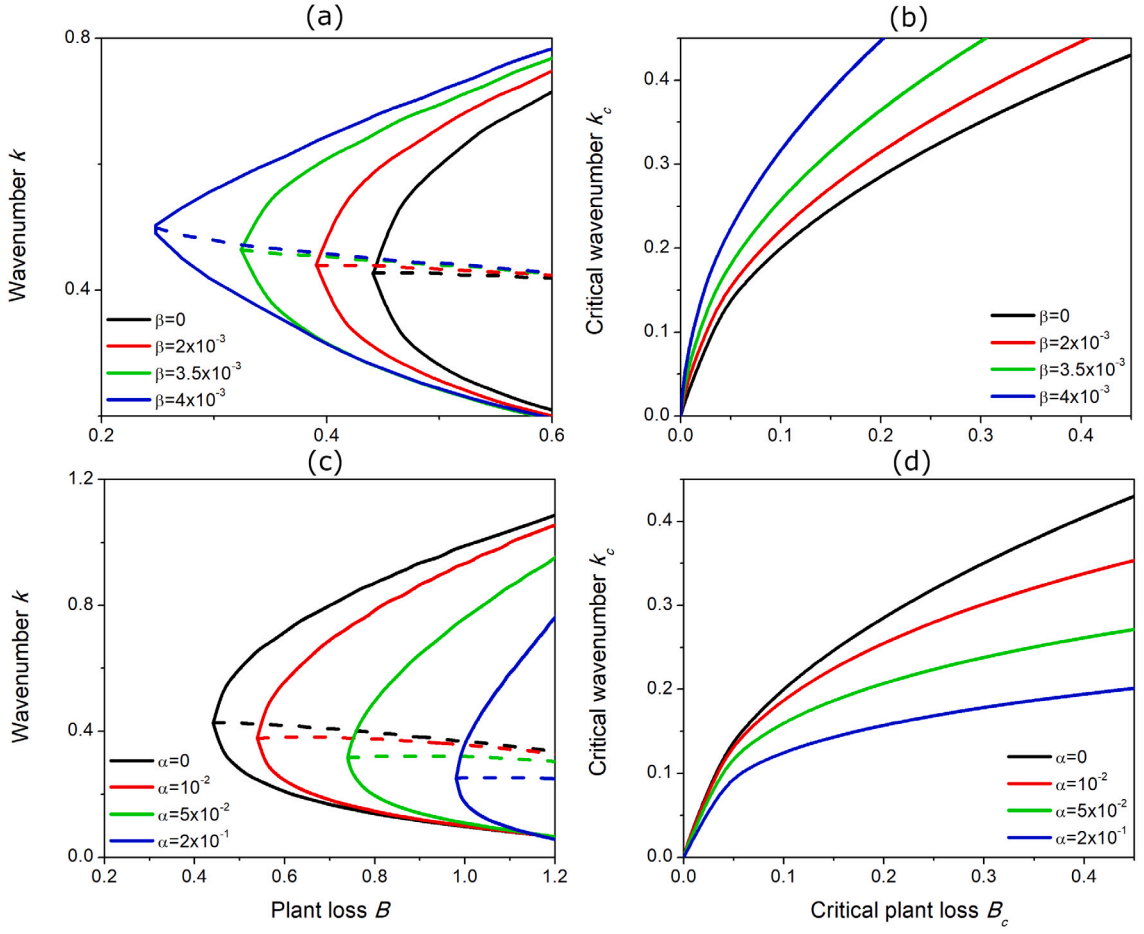

Fig. 2. (a, c) Solid (dashed) lines represent the range of unstable wavenumbers (the most unstable wavenumber) as a function of the plant loss B for different values of β (a) and α (c). (b, d) The critical wavenumber as a function of B_c for different values of β (b) and α (d). Fixed parameters: $d = 500$, $A = 2.8$, $\alpha = 0$ in (a, b) and $\beta = 0$ in (c, d).

the critical wavenumber at the onset of instability are depicted in Fig. 2(b, d). These results show that the increase of β (α) conducts to patterns with smaller (bigger) wavelengths at the onset. From the biological viewpoint, these results suggest that an increment of the capability of roots to suction water from soil conducts a richer scenario and admits several different patterned configurations. This framework is given to the fact that a larger range of the admitted wavenumbers conducts a greater number of the excited modes that correspond to a different number of stripes in the selected domain. On the other hand, the increment of the internal competition between plants has exactly the opposite behavior.

Finally, to better understand the combined effects of cross-diffusion and internal competition on the critical values in Fig. 3 we show the density plot of the critical plant loss B_c $(41)_2$ [panel (a)] and the critical wavenumber k_c $(41)_1$ [panel (b)] in the (β, α)-plane. We note that the level curves, characterizing the above quantities when the cross-diffusion and internal competition rates vary continuously, denote a monotonic behavior and confirm results reported in Fig. 1.

As previously observed, the occurrence of stationary patterns depends on the inertial times through conditions $(38)_{5,6}$ which, once the set of model parameters is fixed, characterize the stability or Turing region in the (τ^u, τ^w)-plane. Therefore, by considering different values of α and β, we depict in Fig. 4(a, c, e) the stability regions at the point P_1 denoted in Fig. 1(a), whereas in Fig. 4(b, d, f) we show the stability [panel (f)] and Turing regions [panels (b, d)] at the configuration P_3 [see Fig. 1(a)]. More precisely, the yellow areas represent the region in which conditions $(38)_{5,6}$ are satisfied. In particular, when both β and α are neglected, conditions $(38)_{5,6}$ provide an upper bound on the allowed inertial time, i.e. $\tau^u < 1/B$ [panels (a, b)], as already observed in [39,57]. Differently, when β is taken into account the upper bound value reduces itself according to the strength of the cross-diffusion coefficient [panels (c, d)], whereas the internal competition one plays the opposite role [panels (e, f)]. Note that, in panels (e, f) the upper bound on the inertial time τ^u is given by $\tau^u_{th} \simeq 10.12$ and $\tau^u_{th} \simeq 5.28$, respectively. It is also interesting to notice that the effect of water inertia τ^w seems to be negligible also for $\beta \neq 0$ and only the vegetation one plays an active role in defining the instability region. Therefore, to gain further insight into this feature, we now perform numerical investigations in the (B, β)-plane by fixing $d = 500$, $\alpha = 0$, $\tau^w = 10^{-4}$, $A = 1.7$. Results shown in Fig. 5 for $\tau^u = 10^{-4}$ in panel (a) and $\tau^u = 4$ in panel (b) reveal that a point that lies in the Turing region may conduct to stationary patterns close to the parabolic limit [panel (a)] whereas prevents their occurrence far from it [panel (b)]. The black solid line herein depicted represents the configuration P_3.

In order to corroborate our analytical predictions, we integrate numerically the governing system (2)–(4), (33) with zero-flux boundary conditions and using small sinusoidal fluctuations about the steady state $\mathbf{U}^*_S$ as initial conditions. Simulations have been carried out by means of MATLAB® [60] over a time window $t \in [0, 200]$ and considering a spatial domain of length $D = 100$. In particular, we inspect the time-space evolution of the vegetation biomass $u(x, t)$ at the points P_1, P_2, and P_3 for different values of the cross-diffusion coefficient β in Fig. 6 and at the points P_4, P_5, and P_6 as the internal competition rate α is varied in Fig. 7.

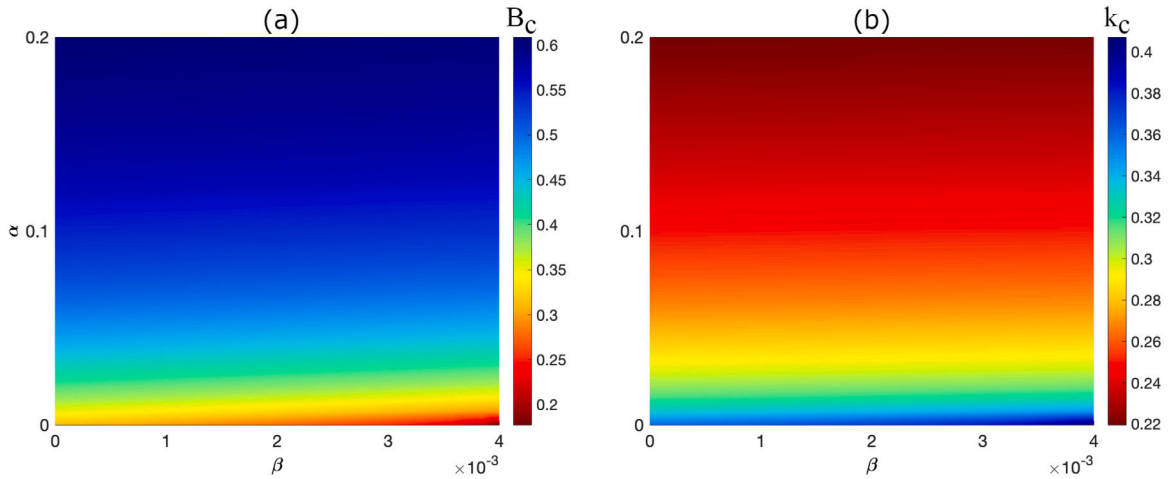

Fig. 3. Density-plot showing the level curves in the (β, α)-plane for the critical threshold B_c (a) and the critical wavenumber k_c (b). Fixed parameters: $d = 500$ and $A = 1.7$.

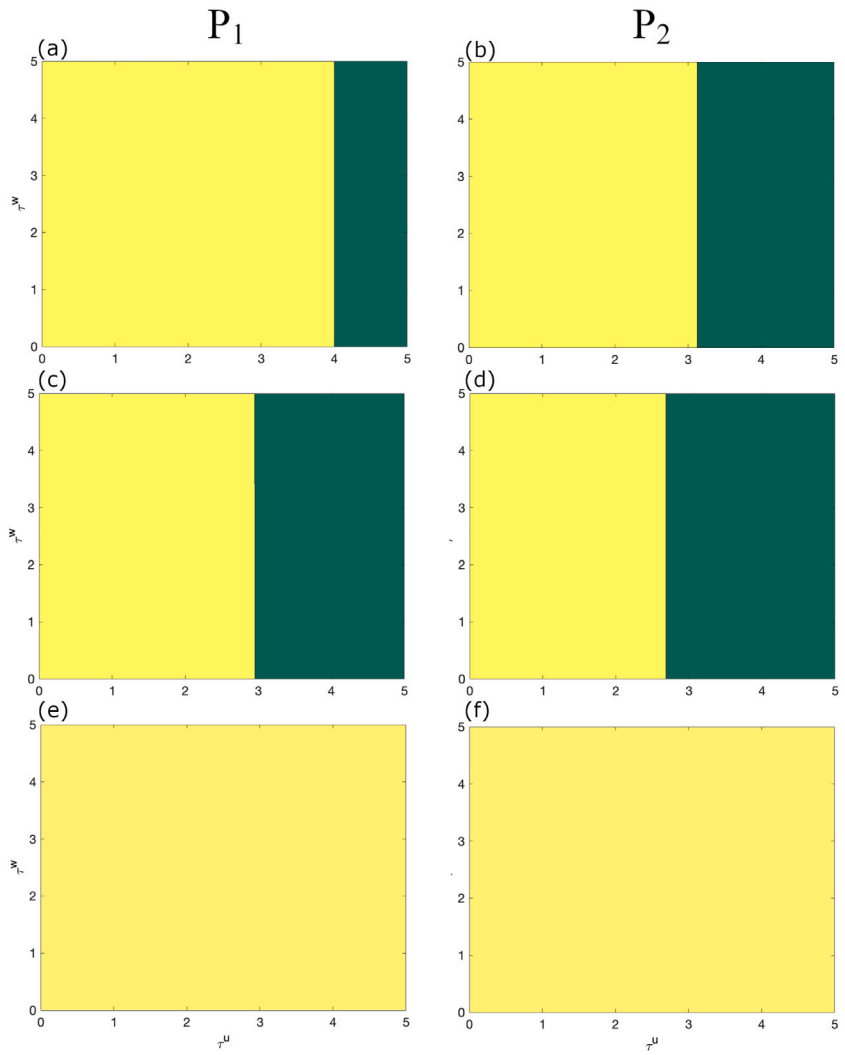

Fig. 4. $\tau^u - \tau^w$ region defined by $(38)_{5,6}$ and obtained for model parameters corresponding to the points P_1 (a, c, e) and P_3 (b, d, f) for different values of β and α. In particular $\beta = 0$ and $\alpha = 0$ in panels (a, b), $\beta = 2 \times 10^{-3}$ and $\alpha = 0$ in panels (c, d), $\beta = 0$ and $\alpha = 10^{-2}$ in panels (e, f). Other fixed parameters: $d = 500$.

According to Fig. 1(a), numerical results shown in Fig. 6 reveal that vegetated stripes are observed only at P_3 [panel (c)] for $\beta = 0$, whereas for $\beta = 2 \times 10^{-3}$ stationary patterns occur at both P_2 and P_3 [panels (e, f)]. Finally, since P_1, P_2 and P_3 are located within the Turing instability region for $\beta = 3.5 \times 10^{-3}$, the system evolves towards band configurations at each of these points [panels (g, h, i)]. On the contrary, the opposite behavior

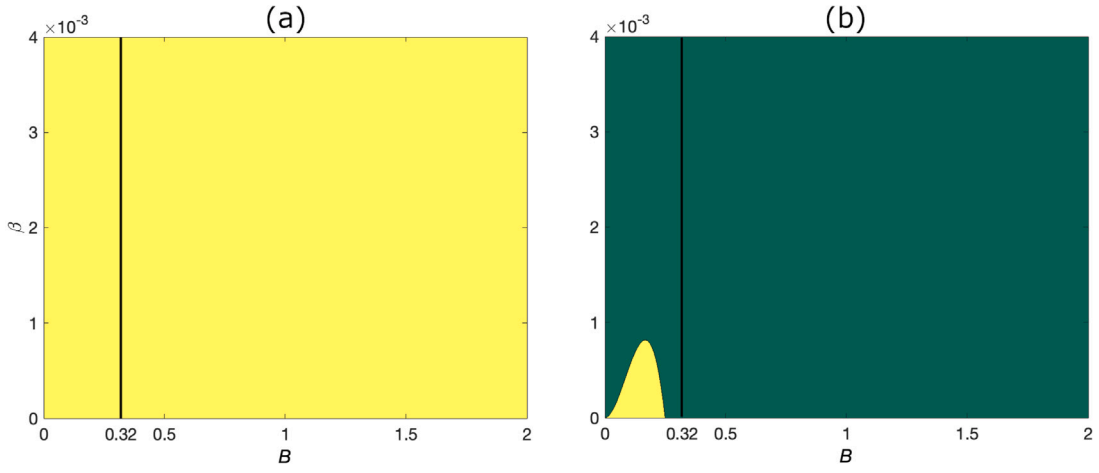

Fig. 5. $B-\beta$ region defined by $(38)_{5,6}$ and obtained for model parameters corresponding to the point P_3 for $\tau^u = 10^{-4}$ (a) and $\tau^u = 4$ (b). Fixed parameters: $d = 500$, $A = 1.7$, $\alpha = 0$ and $\tau^w = 10^{-4}$.

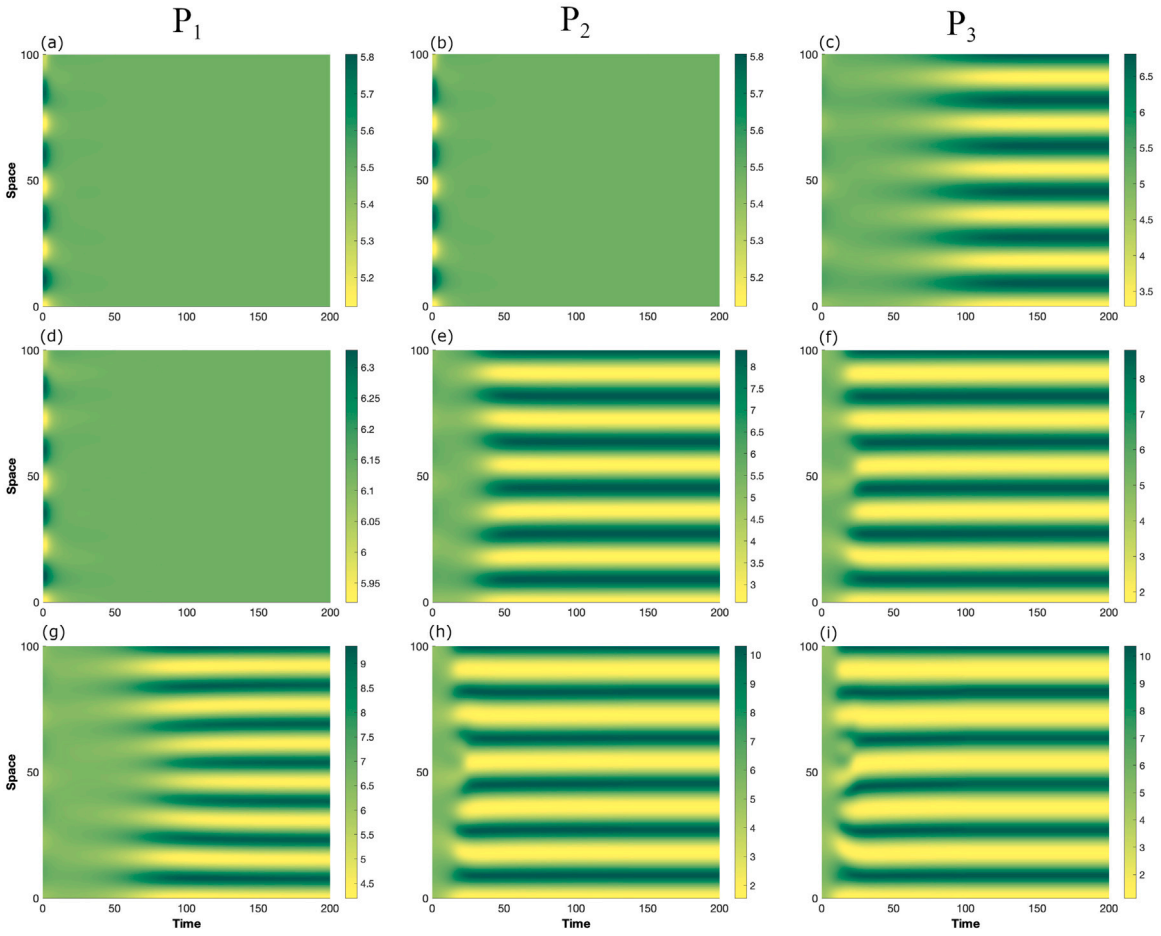

Fig. 6. Spatiotemporal dynamics of vegetation biomass $u(x,t)$ corresponding to P_1 (a, d, g), P_2 (b, e, h) e P_3 (c, f, i) for $\beta = 0$ (a, b, c), $\beta = 2\times10^{-3}$ (d, e, f) and $\beta = 3.5\times10^{-3}$ (g, h, i). Fixed parameters: $\tau^u = \tau^w = 10^{-4}$. Other parameters as in Fig. 1(a).

is observed in Fig. 7 when the internal competition rate is varied. In particular, for $\alpha = 0$ all the considered configurations lead to the occurrence of Turing patterns [panel (a, b, c)], for $\alpha = 10^{-2}$ stripes arise at P_5 and P_6 [panels (e, f)], whereas for $\alpha = 5\times10^{-2}$ vegetation patterns occur at only P_6, confirming the results obtained in Fig. 1(b).

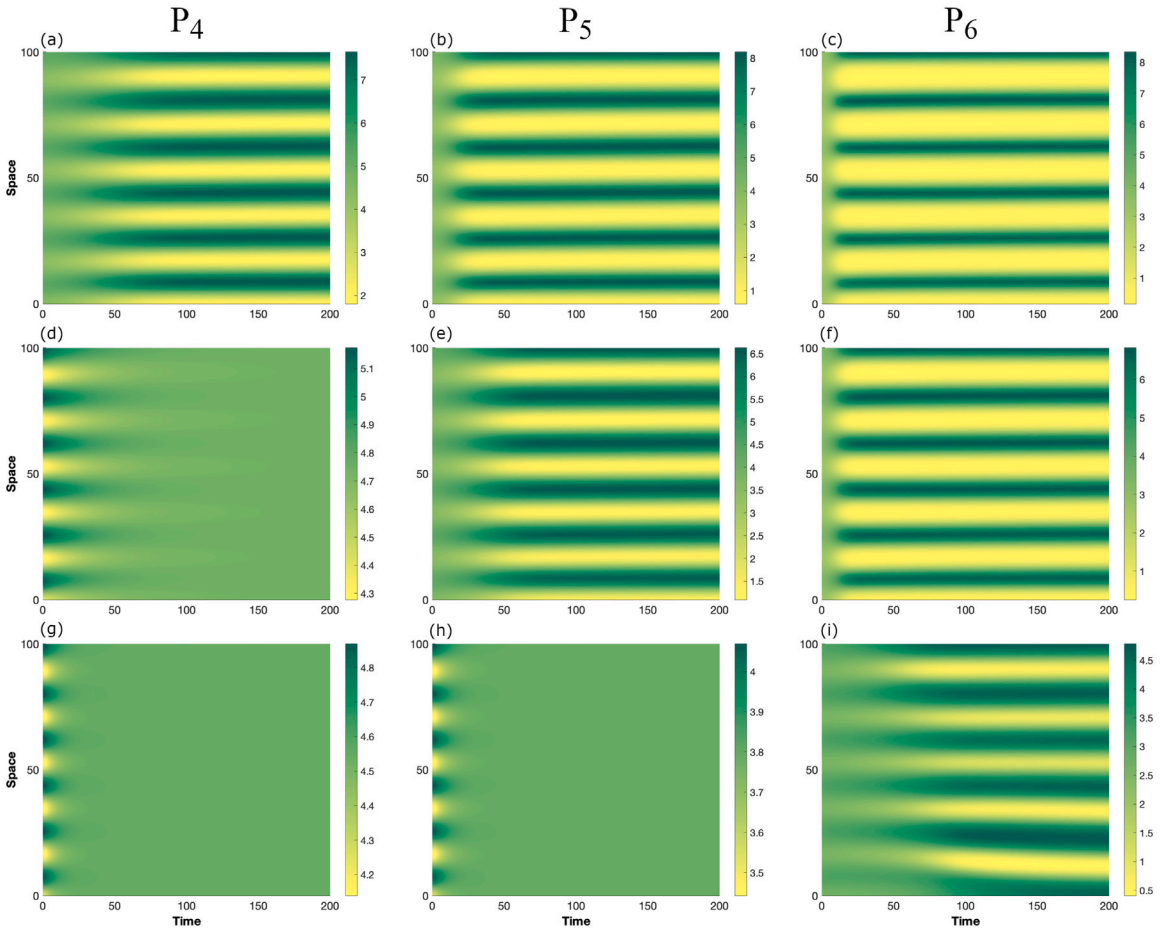

Fig. 7. Spatiotemporal dynamics of vegetation biomass $u(x,t)$ corresponding to P_4 (a, d, g), P_5 (b, e, h) e P_6 (c, f, i) for $\alpha = 0$ (a, b, c), $\alpha = 10^{-2}$ (d, e, f) and $\alpha = 5 \times 10^{-2}$ (g, h, i). Fixed parameters: $\tau^u = \tau^w = 10^{-4}$. Other parameters as in Fig. 1(b).

Next, according to the weakly nonlinear analysis developed in Section 3, we deduce the cubic Stuart–Landau Eq. (22) for the pattern amplitude with

$$\sigma = \frac{B_2\left\{2u_{S_c}^2\left[1+(1+\alpha)u_{S_c}^2\right]\left(2\alpha B_c r_1 - r_2\right)\left(r_1+dr_2-\beta d r_1\right)+B_c r_1\left[1-(1+\alpha)u_{S_c}^2\right]\left(1+\alpha u_{S_c}^2\right)\left[d\left(\beta r_1 - r_2\left(1-\alpha u_{S_c}^2\right)\right)-2r_1\right]\right\}}{B_c r_1\left[1-(1+\alpha)u_{S_c}^2\right]\left(1+\alpha u_{S_c}^2\right)^2\left\{r_2+d\left(r_2-\beta r_1\right)\left[k_c^2(\tau^u-\tau^w)-1\right]\right\}},$$
$$L = \frac{\left(p_1+8q_1+4s_1\right)\left(r_1+dr_2-\beta d r_1\right)}{8r_1\left\{r_2+d\left(r_2-\beta r_1\right)\left[k_c^2(\tau^u-\tau^w)-1\right]\right\}}, \tag{42}$$

being

$$p_1 = \frac{6r_1^2\left[4\alpha B_c r_1\left(\alpha u_{S_c}^2-1\right)+r_2\left(1-3\alpha u_{S_c}^2\right)\right]}{\left(1+\alpha u_{S_c}^2\right)^3},$$
$$q_1 = \frac{2n_1\left[B_c r_1\left(1-u_{S_c}^2-3\alpha u_{S_c}^2\right)+r_2 u_{S_c}^2\right]}{u_{S_c}\left(1+\alpha u_{S_c}^2\right)^2},$$
$$s_1 = \frac{2n_1\left\{r_1\left[B_c\left(1-u_{S_c}^2-3\alpha u_{S_c}^2\right)+4dB_c k_c^2+4k_c^2 u_{S_c}^2(\beta d-1-3\alpha d B_c)\right]+r_2 u_{S_c}^2\left(1+4dk_c^2\right)\right\}}{9u_{S_c}\left(1+\alpha u_{S_c}^2\right)^2}, \tag{43}$$
$$n_1 = \frac{r_1^2\left(2k_c^2-B_c\right)}{2u_{S_c}B_c\left[(1+\alpha)u_{S_c}^2-1\right]}.$$

Then, in order to investigate when $\mathbf{U}_S^*$ undergoes to a supercritical ($L > 0$) or subcritical bifurcation ($L < 0$), we depict in Fig. 8 the dependence of the Landau coefficient L $(42)_2$ as a function of the critical plant loss B_c, for different values of τ^w [panel (a)], β [panel (b)] and α [panel (c)]. A direct inspection of Fig. 8(a) confirms that the inertial times τ^u and τ^w do not affect the zeros of L, as it can be seen in $(42)_2$. Moreover, panel (b) reveal that the cross-diffusion favors the supercritical regime due to the fact that the transition threshold from subcritical to the supercritical

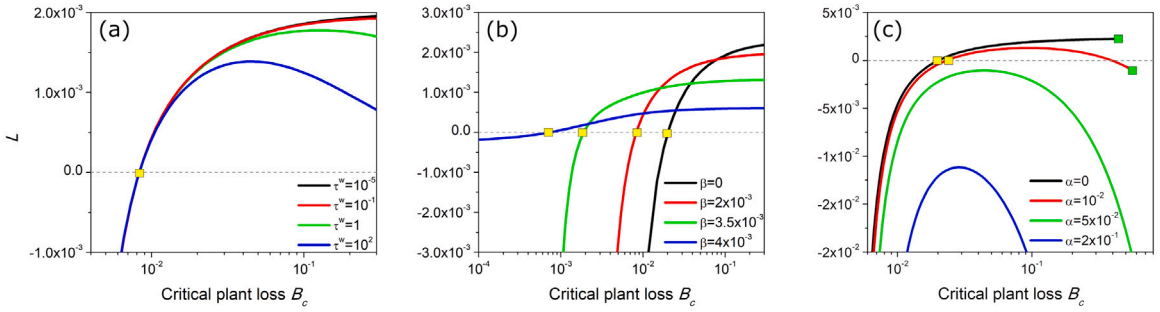

Fig. 8. Dependence of the parameter L as a function of the critical plant loss B_c for $d = 500$ and $\tau^u = 10^{-4}$. The condition $L = 0$ separates the supercritical regime ($L > 0$) from the subcritical one ($L < 0$). Other parameters: $\alpha = 0$ in (a, b), $\tau^w = 10^{-4}$ in (b, c), $\beta = 2 \times 10^{-3}$ in (a) and $\beta = 0$ in (c).

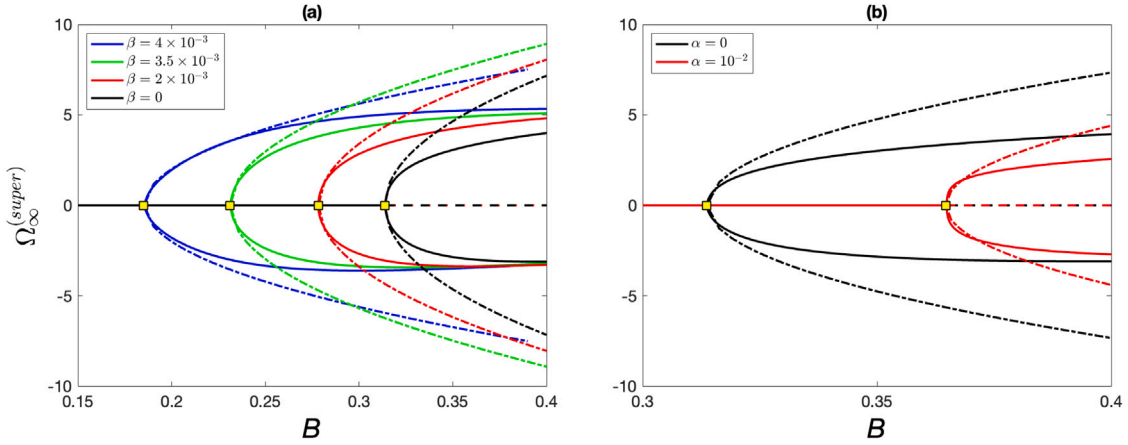

Fig. 9. The bifurcation diagram in the supercritical case showing the amplitude of different stationary states $\Omega_\infty^{(super)}$ as a function of the plant loss B. Solid and dashed-dotted lines represent the stable branches obtained analytically by weakly nonlinear analysis (25) and numerically via XPPAUT, respectively. The dashed line depicts the unstable branch. The critical plant loss values B_c are denoted by squares. Fixed parameters: $A = 1.7$, $\alpha = 0$ (a) and $\beta = 0$ (b).

regime (yellow squares) occurs for smaller values of plant loss B as β increases. On the contrary, the internal competition gives advantages to the subcritical dynamics, i.e. the transition point occurs for greater values of B when α is increased. More precisely, when the internal competition is neglected subcritical dynamics occur only for small values of critical plant loss B_c whereas when α increases the subcritical region enlarges itself. From the ecological viewpoint, it is possible to conclude that, at least in the considered parameter setup, the increment of the capability of plants' roots to suction water from the soil (plants' internal competition) makes the vegetation pattern less (more) resilient to the variation of plant loss.

Let us now focus on the dynamics occurring in the supercritical regime ($L > 0$). As already observed in Section 3, the asymptotic value of the pattern amplitude $\Omega_\infty^{(\text{super})}$ (25) depends on the model parameters, but it is not affected by the inertial times. Therefore, for different values of β and α, we plot in Fig. 9 the analytical (solid lines) and numerical (dashed-dotted ones) bifurcation diagram obtained via weakly nonlinear analysis and the bifurcation package XPPAUT [61], respectively. Notice that, since σ and L are positive, in both cases a supercritical pitchfork bifurcation arises and the pattern amplitude follows a square root law for $B > B_c$. Moreover, a direct inspection of this figure reveals that the comparison between the analytical and the numerical results agrees well close to the onset of instability whereas became worst when the distance from the threshold is increased, as expected by weakly non-linear analysis. Finally, it can be observed that the bifurcation threshold occurs for smaller (greater) values of the plant loss B as β (α) increases and, in turn, vegetated bands with larger (smaller) amplitudes appear accordingly to the fact that the distance from the threshold is varied. These behaviors, which are consistent with the results depicted in Fig. 1(a) and Fig. 3, are also confirmed by numerical simulation [Fig. 10(a, b, d, e)] performed by integrating the governing system (2)–(4), (33). Then, in Fig. 10(c, f) we plot the comparison among the time evolution of the theoretical (27) (solid lines) and numerical (dashed ones) envelopes of vegetation patterns obtained for the parameter setting as in panels (a, b, d, e). Results provide a good agreement for $\beta = 2 \times 10^{-3}$ and $\alpha = 10^{-2}$, whereas it becomes worst from a quantitative viewpoint for $\beta = 3.5 \times 10^{-3}$ and $\alpha = 0$, since these latter cases describe far-from-threshold dynamics.

Finally, we inspect the role of the inertial times on the supercritical transient regime. First, in Fig. 11(a, b, c) we fix τ^u and we choose two different values of τ^w, i.e $\tau^w = 10^{-3}$ and $\tau^w = 5$, corresponding to the dynamics occurring close and far from the parabolic limit respectively. These results confirm that the hyperbolicity does not affect the pattern amplitude whereas it enlarges the transient regime, namely more time is needed to reach the equilibrium pattern. On the contrary, according to the analytical prediction (23), if the inertial times offset with each other $\tau^u = \tau^w$, Fig. 11(d, e, f) shows that the hyperbolic model exhibits exactly the same transient dynamic of the corresponding parabolic system. However, in this framework, working with a hyperbolic reaction-transport model is useful to better describe the transient regimes. In particular, inertia plays a non-trivial role in those dynamics that are characterized by long-time evolutions, such as the vegetation ones which, for instance, evolve over centuries in the case of tree dynamics.

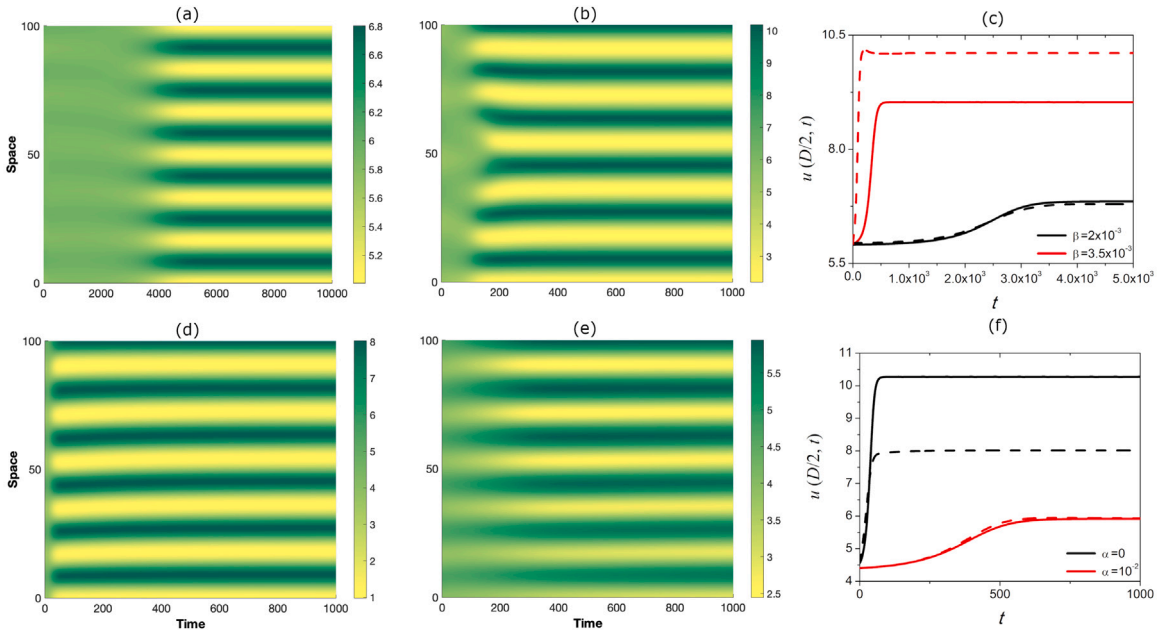

Fig. 10. Spatio-temporal evolution of vegetation patterns in the supercritical regime obtained for $\beta = 2 \times 10^{-3}$ (a), $\beta = 3.5 \times 10^{-3}$ (b), $\alpha = 0$ (d) and $\alpha = 10^{-2}$ (e). Panels (c, f) show the comparison among the time evolution of the theoretical (solid lines) and numerical (dashed ones) envelopes of vegetation patterns obtained in the above cases. Fixed parameters: $A = 1.7$, $B = 0.28$ in (a, b, c), $B = 0.37$ in (d, e, f), $\tau^u = \tau^w = 10^{-4}$, $d = 500$, $\alpha = 0$ in (a, b) and $\beta = 0$ in (d, e).

We now focus our attention on the subcritical regime where the evolution of pattern amplitude is ruled by the quintic Stuart-Landau Eq. (28) with

$$\begin{aligned}
\widetilde{\sigma} = & \frac{1}{2r_1\left\{r_2 + d\left(\beta r_1 - r_2\right)\left[1 - k_c^2\left(\tau^u - \tau^w\right)\right]\right\}} \times \\
& \times \left\{ \left(\beta d r_1 - r_1 - d r_2\right)\left[2\left(\omega_{10}B_2 + B_4 r_1\right)\frac{\mathrm{d}f_u^*}{\mathrm{d}B} + 2\left(\omega_{20}B_2 + B_4 r_2\right)\frac{\mathrm{d}f_w^*}{\mathrm{d}B} + B_2^2\left(r_1\frac{\mathrm{d}^2 f_u^*}{\mathrm{d}B^2} + r_2\frac{\mathrm{d}^2 f_w^*}{\mathrm{d}B^2}\right)\right] \right. \\
& \left. + 2\sigma\left[d\left(r_2 - \beta r_1\right)\left(\omega_{10} - \omega_{30}k_c\tau^u\right) - r_1\left(\omega_{20} - k_c\omega_{40}\tau^w\right)\right] - 2r_1\left(\omega_{10}B_2 + B_4 r_1\right)\right\}, \qquad (44) \\
\widetilde{L} = & \frac{B_2\left(r_1 + d r_2 - \beta d r_1\right)\left\{4\left(m_1 + 2n_1\right)\left(r_2\frac{\mathrm{d}f_{uw}^*}{\mathrm{d}B} + r_1\frac{\mathrm{d}f_{uu}^*}{\mathrm{d}B}\right) + 4r_1\left(m_2 + 2n_2\right)\frac{\mathrm{d}f_{uw}^*}{\mathrm{d}B} + 8\left(\omega_{21}\frac{\mathrm{d}f_w^*}{\mathrm{d}B} + \omega_{11}\frac{\mathrm{d}f_u^*}{\mathrm{d}B}\right) + r_1^2\left(r_1\frac{\mathrm{d}f_{uuu}^*}{\mathrm{d}B} + 3r_2\frac{\mathrm{d}f_{uuw}^*}{\mathrm{d}B}\right)\right\}}{8r_1\left\{r_2 + d\left(\beta r_1 - r_2\right)\left[1 - k_c^2\left(\tau^u - \tau^w\right)\right]\right\}} + \\
& + \frac{\left(r_1 + d r_2 - \beta d r_1\right)}{8r_1\left\{r_2 + d\left(\beta r_1 - r_2\right)\left[1 - k_c^2\left(\tau^u - \tau^w\right)\right]\right\}}\left\{\omega_{20}\left[3r_1^2 f_{uuw}^* + 4\left(m_1 + 2n_1\right)f_{uw}^*\right] + 2\omega_{10}\left[3r_1 r_2 f_{uuw}^* + \right.\right. \\
& \left. + 2\left(m_2 + 2n_2\right)f_{uw}^* + 2\left(m_1 + 2n_1\right)f_{uu}^*\right] + 4r_1 f_{uw}^*\left(2\zeta_{20} + \zeta_{22}\right) + 4\left(r_2 f_{uw}^* + r_1 f_{uu}^*\right)\left(2\zeta_{10} + \zeta_{12}\right)\right\} + \qquad (45) \\
& + \frac{1}{r_1\left\{r_2 + d\left(\beta r_1 - r_2\right)\left[1 - k_c^2\left(\tau^u - \tau^w\right)\right]\right\}}\left\{B_2 r_1\omega_{11} - 3\sigma\left[d\left(r_2 - \beta r_1\right)\left(\omega_{11} - k_c\omega_{31}\tau^u\right) - r_1\left(\omega_{21} - k_c\omega_{41}\tau^w\right)\right]\right. \\
& \left. + L\left[d\left(r_2 - \beta r_1\right)\left(\omega_{10} - k_c\omega_{30}\tau^u\right) - r_1\left(\omega_{20} - k_c\tau^w\omega_{40}\right)\right]\right\}, \\
\widetilde{R} = & -\frac{\left(r_1 + d r_2 - \beta d r_1\right)}{8r_1\left\{r_2 + d\left(\beta r_1 - r_2\right)\left[1 - k_c^2\left(\tau^u - \tau^w\right)\right]\right\}}\left\{\omega_{23}\left(r_1^2 f_{uuw}^* + 4m_1 f_{uw}^*\right) + \omega_{13}\left[r_1\left(r_1 f_{uuu}^* + 2r_2 f_{uuw}^*\right) + \right.\right. \\
& + 4\left(m_2 f_{uw}^* + m_1 f_{uu}^*\right)\left] + \omega_{21}\left[3r_1^2 f_{uuw}^* + 4\left(m_1 + 2n_1\right)f_{uw}^*\right] + \omega_{11}\left[3r_1\left(r_1 f_{uuu}^* + 2r_2 f_{uuw}^*\right) + \right. \\
& + 4\left(m_2 + 2n_2\right)f_{uw}^* + 4\left(m_1 + 2n_1\right)f_{uu}^*\right] + 4\left(r_2 f_{uw}^* + r_1 f_{uu}^*\right)\left(2\eta_{10} + \eta_{12}\right) + 4r_1 f_{uw}^*\left(2\eta_{20} + \eta_{22}\right) + \\
& + 2\left(m_1^2 + 2n_1 m_1 + 2n_1^2\right)\left(r_1 f_{uuu}^* + r_2 f_{uuw}^*\right) + 4r_1\left[\left(m_1 + n_1\right)\left(m_2 + n_2\right) + n_1 n_2\right]f_{uuw}^* + \qquad (46) \\
& + \frac{r_1^2}{3}\left[\left(2m_1 + 3n_1\right)\left(r_1 f_{uuuu}^* + 3r_2 f_{uuuw}^*\right) + r_1\left(2m_2 + 3n_2\right)f_{uuuw}^*\right] + \frac{r_1^4}{24}\left(r_1 f_{uuuuu}^* + 5r_2 f_{uuuuw}^*\right)\left.\right\} + \\
& - \frac{3L\left[d\left(r_2 - \beta r_1\right)\left(\omega_{11} - k_c\omega_{31}\tau^u\right) - r_1\left(\omega_{21} - k_c\omega_{41}\tau^w\right)\right]}{r_1\left\{r_2 + d\left(\beta r_1 - r_2\right)\left[1 - k_c^2\left(\tau^u - \tau^w\right)\right]\right\}}
\end{aligned}$$

and the expression of the coefficients herein occurring are given in the Appendix. As it can be easily observed, the asymptotic amplitude in the subcritical regime $\Omega_\infty^{(\mathrm{sub})}$ (30) depends on the model parameters as well as on the dimensionless distance from the threshold and on the relaxation times. Therefore, unlike the supercritical regime, the weakly nonlinear analysis predicts that the hyperbolic structure of the model may also affect the asymptotic subcritical dynamics. However, as it is well-known, any stationary solutions of the hyperbolic model (2)–(4) must be unaffected by inertial effects [39]. Indeed, this contradiction arises because our analysis starts to fail for patterns with non-negligible amplitude at the onset of instability, namely $O(1)$ perturbation of the uniform steady state. Owing to the nontrivial expressions of (44)–(46), the hyperbolic effects, as well as the cross-diffusion and internal competition ones, are investigated by performing numerical simulations.

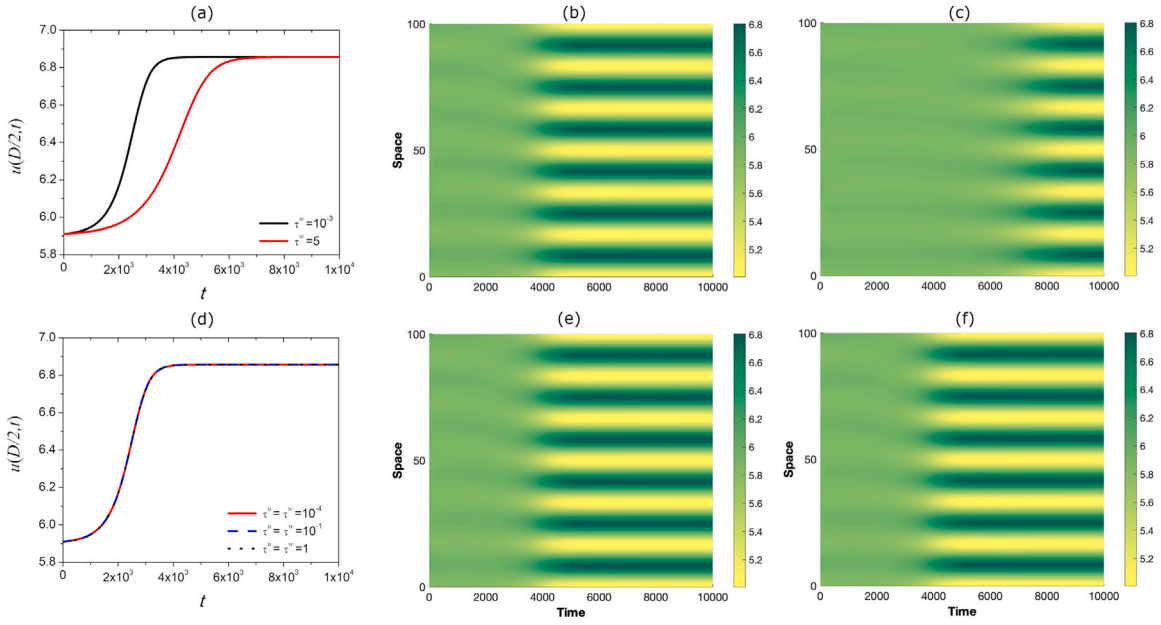

Fig. 11. Spatio-temporal evolution of vegetation patterns in the supercritical regime obtained for $(\tau^u, \tau^w) = (10^{-4}, 10^{-3})$ (b), $(\tau^u, \tau^w) = (10^{-4}, 5)$ (c), $(\tau^u, \tau^w) = (10^{-4}, 10^{-4})$ (c) and $(\tau^u, \tau^w) = (1, 1)$ (c). Panels (a, b) show the comparison among the time evolution of the envelopes of vegetation patterns for $x = D/2$ obtained for $\tau^w = 10^{-3}$ and $\tau^w = 5$ in (a), whereas $\tau^u = \tau^w = 10^{-4}$, $\tau^u = \tau^w = 10^{-1}$ and $\tau^u = \tau^w = 1$ in (b). Fixed parameters: $A = 1.7$, $B = 0.28$, $\beta = 2 \times 10^{-3}$, $\alpha = 0$ and $d = 500$.

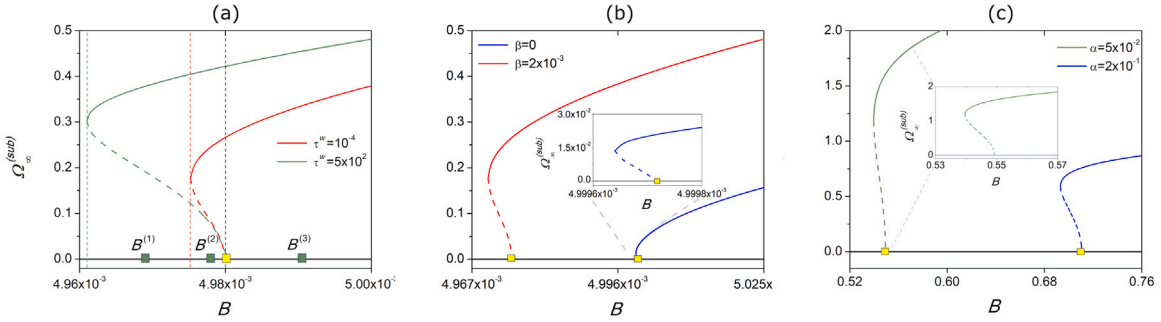

Fig. 12. Bifurcation diagram in the subcritical case for different values of τ^w (a), β (b) and α (c). Solid and dashed lines correspond to stable and unstable branches, respectively. Fixed parameters: $d = 500$, $\tau^u = 10^{-4}$, $\beta = 2 \times 10^{-3}$ in (a) and $\tau^w = 10^{-4}$ in (b, c). In panels (a, b) we fix $A = 0.01$ and $\alpha = 0$, whereas in panel (c) $A = 2$ and $\beta = 0$.

To this aim, the bifurcation diagram in the $(B, \Omega_\infty^{(sub)})$-plane is depicted in Fig. 12 by fixing $d = 500$ and $\tau^u = 10^{-4}$ for different values of τ^w, β and α. This figure highlights the interesting phenomenon of hysteresis described by the quintic Stuart–Landau equation and characteristic of the subcritical regime. In fact, Fig. 12 shows that two qualitatively stable states exist for $B_s < B < B_c$, being B_s the turning point in the backward bifurcation. In detail, the corresponding results depicted in panel (a) show a sensitivity of B_s on the relaxation times, in fact it decreases for bigger values of τ^w by keeping fixed the instability threshold. Differently, when β (α) is varied [see panels (b, c)] the bifurcation threshold occurs for lower (greater) values of plant loss B, so that the stationary amplitude is strongly affected by both the cross-diffusion coefficient and the internal competition rate.

Therefore, to validate the above scenario, we integrate numerically the hyperbolic system (1), (33) in the ranges $t \in [0, 10^5]$ and $x \in [0, 500]$. Note that, we have to enlarge both time and space scales because subcritical modes are characterized by longer dynamics and greater wavelength with respect to the supercritical ones. Results are shown in Fig. 13 for $\tau^w = 10^{-4}$ [panels (a, b, c)] and $\tau^w = 5 \times 10^2$ [panels (d, e, f)]. In particular, starting with an above-threshold value corresponding to $B^{(3)} > B_c$, depicted in Fig. 12(a), the solution stabilizes to a pattern with the amplitude corresponding to the stable branch of the bifurcation diagram, as it is shown in Fig. 13(a, d). Then, by decreasing B below B_c at the value corresponding to $B^{(2)}$ ($B_s < B < B_c$), labeled in Fig. 12(a), the pattern still survives [Fig. 13(b, e)], whereas at $B^{(1)} < B_s$ vegetation bands disappear in both setups [Fig. 13(c, f)]. This latter result confirms that the enlargement of the instability region due to hyperbolicity is an artifact of the weakly nonlinear expansion [39,62].

Moreover, it should be noticed that, as expected by weakly nonlinear analysis, the saddle node predicted by Eq. (30) is not exactly fitted by theoretical results because it is not close enough to the onset of instability and its approximation starts to become not satisfying. This observation is validated by the comparison between the theoretical and numerical bifurcation diagrams depicted in Fig. 14 for the model parameters as in the inset of Fig. 12(c). In particular, it shows that theoretical predictions agree well to numerical results close to the onset of instability and the agreement

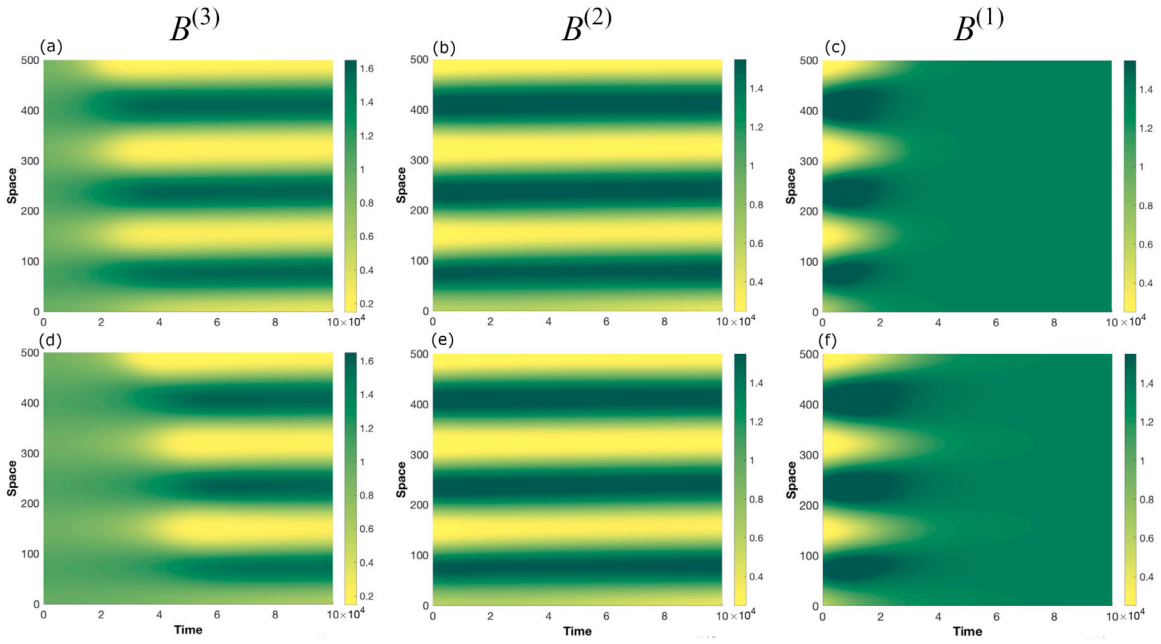

Fig. 13. Spatio-temporal evolution of vegetation patterns in the subcritical regime obtained for $B^{(1)}$ (a, d), $B^{(2)}$ (b, e) and $B^{(3)}$ (c, f) by considering $\tau^{w} = 10^{-4}$ (a, b, c) and $\tau^{w} = 5\times10^{2}$ (d, e, f). Other parameters as in Fig. 12(a).

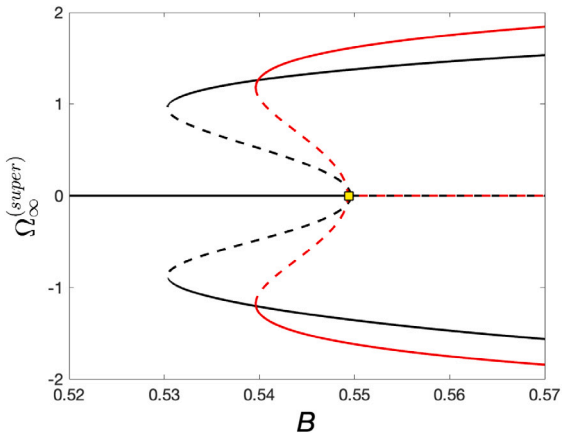

Fig. 14. Bifurcation diagrams for the model parameters as in the inset of Fig. 12(c). Solid (dashed) lines represent the stable (unstable) branches. The red (black) lines denote the analytical (numerical) bifurcation diagram obtained via weakly nonlinear analysis (the software XPPAUT). The critical plant loss value B_c is denoted by the yellow square. (For interpretation of the references to color in this figure legend, the reader is referred to the web version of this article.)

becomes unsatisfactory when the distance from the threshold is increased. Therefore, in the subcritical regimes the theoretical bifurcation diagrams obtained by using weakly nonlinear analysis give us a qualitative, but not quantitative, result.

5. Conclusion

In this manuscript, the occurrence of stationary vegetation patterns on flat terrains is theoretically investigated for a 1D hyperbolic class of reaction-transport systems. In particular, the model here considered includes a cross-diffusion term as well as inertial times. The former has been introduced to account for the process of water uptake by plant roots which assume a fundamental role in resource redistribution in arid and semiarid environments. The latter has to be taken into account in order to describe accurately the transient regime as well as the transition between patterned states or uniformly vegetated states and periodic ones.

In order to describe how these phenomena affect vegetation dynamics, the linear stability analysis has been performed by deducing the main features characterizing stationary patterns at the onset of instability, so that the condition under which Turing instability occurs has been derived. Then, to gain some insight into the pattern dynamics as well as to describe the transient regime, the equation ruling the pattern amplitude evolution close to the onset of instability has been obtained in both supercritical and subcritical regimes by means of weakly nonlinear analysis.

All the analytical predictions were corroborated by numerical simulations in the illustrative example of a modified Klausmeier model. The extension here considered takes into account the internal competition of plants that, in arid and semiarid environments, plays a crucial role in plant survival. Therefore, the effects of the cross-diffusion as well as the internal competition rate and the inertial times have been here illustrated.

Results suggest that the cross-diffusion term has a destabilizing effect by enlarging the region in which patterns may be observed and by favoring the occurrence of supercritical dynamics. In particular, it is able to: (i) shift up the locus at which Turing instability occurs, (ii) decrease the vegetation stripes' wavelength and (iii) decrease the plant loss value beyond which the supercritical regime is observed. On the contrary, the internal competition rate plays exactly the opposite role and enlarges the region in which only the desert state exists. Finally, the inertial times are able to modulate the transient regime and prevent the occurrence of stationary vegetation patterns playing a crucial role in the description of those phenomena occurring over different timescales. Furthermore, we observed that the dynamics obtained in the parabolic regime can be recovered not only for vanishing inertial times but also when they offset each other.

The mathematical results herein obtained are consistent with the biological framework and may be very useful in extracting additional information about ecosystem resilience and its response to a loosing of environmental conditions, such as an increase in plant loss, inner competition or roots' suction. Furthermore, the occurrence of inertia may suggest also a great impact on those dynamics characterized by time-dependent parameters in which transient regimes play a more crucial role. In our opinion, the manuscript may attract both the interest of ecologists and mathematicians involved in the study of vegetation patterned dynamics in arid and semi-arid environments on flat terrains. In particular, the model here considered is able to include several ecological observations that better mimic the real physical process of plant evolution. In this context, the mathematical tools here developed play a very important role in better characterizing the vegetation response to a stressor and in preventing possible ecological disasters.

Finally, this paper should be read as a first step versus the analysis of more complex phenomena, such as the occurrence of oscillatory vegetation patterns, the emergence of transitions between different patterned configurations, and the study of far-from-threshold dynamics.

CRediT authorship contribution statement

C. Currò: Conceptualization, Methodology, Formal analysis, Investigation, Writing – original draft, Writing – review & editing, Supervision, Funding acquisition. **G. Grifò:** Software, Methodology, Formal analysis, Investigation, Writing – original draft, Writing – review & editing. **G. Valenti:** Conceptualization, Methodology, Formal analysis, Investigation, Writing – original draft, Writing – review & editing, Supervision, Funding acquisition.

Declaration of competing interest

The authors declare that they have no known competing financial interests or personal relationships that could have appeared to influence the work reported in this paper.

Data availability

No data was used for the research described in the article.

Acknowledgments

This research was funded by MUR (Italian Ministry of University and Research) through PRIN2017 Project No. 2017YBKNCE, "Multiscale phenomena in Continuum Mechanics: singular limits, off-equilibrium and transitions" and by INdAM-GNFM.

Appendix. Derivation of the quintic Stuart–Landau equation

In this Appendix we provide some details about the derivation of the quintic Stuart–Landau Eq. (28) obtained by pushing the analysis performed in Section 3 up to the fifth order. As already observed, the cubic Stuart–Landau Eq. (22) for the amplitude Ω still holds, even though the derivative with respect T_2 is now a partial derivative. Then, the solution of Eq. $(15)_3$ is given by

$$\mathbf{U}_3 = \Omega \begin{bmatrix} \left(\mathbf{U}_{31} + \Omega^2 \mathbf{U}_{32}\right) \cos\left(k_c\, x\right) + \Omega^2 \mathbf{U}_{33} \cos\left(3k_c\, x\right) \\ \left(\widehat{\mathbf{U}}_{31} + \Omega^2 \widehat{\mathbf{U}}_{32}\right) \sin\left(k_c\, x\right) + \Omega^2 \widehat{\mathbf{U}}_{33} \sin\left(3k_c\, x\right) \end{bmatrix} \tag{A.1}$$

where the vectors

$$\begin{aligned} &\mathbf{U}_{31} = \begin{bmatrix} \omega_{10} \\ \omega_{20} \end{bmatrix}, \quad \mathbf{U}_{32} = \begin{bmatrix} \omega_{11} \\ \omega_{21} \end{bmatrix}, \quad \mathbf{U}_{33} = \begin{bmatrix} \omega_{13} \\ \omega_{23} \end{bmatrix} \\ &\widehat{\mathbf{U}}_{31} = \begin{bmatrix} \omega_{30} \\ \omega_{40} \end{bmatrix}, \quad \widehat{\mathbf{U}}_{32} = \begin{bmatrix} \omega_{31} \\ \omega_{41} \end{bmatrix}, \quad \widehat{\mathbf{U}}_{33} = \begin{bmatrix} \omega_{33} \\ \omega_{43} \end{bmatrix} \end{aligned} \tag{A.2}$$

satisfy the following systems

$$\begin{aligned} &\left(k_c^2 \mathbf{D} - \widetilde{\nabla}\mathbf{F}\right)_c^* \mathbf{U}_{31} = k_c \sigma \boldsymbol{\Lambda} \hat{\mathbf{r}} - \sigma \mathbf{r} + B_2 \mathbf{t} \\ &\left(k_c^2 \mathbf{D} - \widetilde{\nabla}\mathbf{F}\right)_c^* \mathbf{U}_{32} = \tfrac{1}{8}\left(\mathbf{p} + 4\mathbf{s} + 8\mathbf{q}\right) + L\left(\mathbf{r} - k_c \boldsymbol{\Lambda} \hat{\mathbf{r}}\right) \\ &\left(9k_c^2 \mathbf{D} - \widetilde{\nabla}\mathbf{F}\right)_c^* \mathbf{U}_{33} = \tfrac{1}{24}\left(\mathbf{p} + 12\mathbf{s}\right) \\ &\widehat{\mathbf{U}}_{31} = \frac{1}{k_c}\left[\left(\widetilde{\nabla}\mathbf{F}\right)_c^* \mathbf{U}_{31} - \sigma \mathbf{r} + B_2 \mathbf{t}\right] \\ &\widehat{\mathbf{U}}_{32} = \frac{1}{k_c}\left[\left(\widetilde{\nabla}\mathbf{F}\right)_c^* \mathbf{U}_{32} + L\mathbf{r} + \tfrac{1}{8}\left(\mathbf{p} + 4\mathbf{s} + 8\mathbf{q}\right)\right] \\ &\widehat{\mathbf{U}}_{33} = 3k_c \mathbf{D}\, \mathbf{U}_{33} \end{aligned} \tag{A.3}$$

with

$$\mathbf{\Lambda} = \begin{bmatrix} \tau^u & 0 \\ 0 & \tau^w \end{bmatrix} \tag{A.4}$$

Substituting (16), (19), (A.1) into $(15)_4$ we obtain

$$\mathbf{U}_4 = \Omega^2 \begin{bmatrix} \mathbf{U}_{40} + \Omega^2 \mathbf{U}_{41} + \left(\mathbf{U}_{42} + \Omega^2 \mathbf{U}_{43}\right) \cos\left(2k_c\, x\right) + \Omega^2 \mathbf{U}_{44} \cos\left(4k_c\, x\right) \\ \left(\hat{\mathbf{U}}_{42} + \Omega^2 \hat{\mathbf{U}}_{43}\right) \sin\left(2k_c\, x\right) + \Omega^2 \hat{\mathbf{U}}_{44} \sin\left(4k_c\, x\right) \end{bmatrix} \tag{A.5}$$

where the vectors

$$\begin{aligned} &\mathbf{U}_{40} = \begin{bmatrix} \zeta_{10} \\ \zeta_{20} \end{bmatrix}, \mathbf{U}_{41} = \begin{bmatrix} \eta_{10} \\ \eta_{20} \end{bmatrix}, \mathbf{U}_{42} = \begin{bmatrix} \zeta_{12} \\ \zeta_{22} \end{bmatrix}, \mathbf{U}_{43} = \begin{bmatrix} \eta_{12} \\ \eta_{22} \end{bmatrix} \\ &\hat{\mathbf{U}}_{42} = \begin{bmatrix} \zeta_{32} \\ \zeta_{42} \end{bmatrix}, \hat{\mathbf{U}}_{43} = \begin{bmatrix} \eta_{32} \\ \eta_{42} \end{bmatrix}, \mathbf{U}_{44} = \begin{bmatrix} \eta_{14} \\ \eta_{24} \end{bmatrix}, \hat{\mathbf{U}}_{44} = \begin{bmatrix} \eta_{34} \\ \eta_{44} \end{bmatrix} \end{aligned} \tag{A.6}$$

are obtained by solving the following systems

$$\begin{aligned} &\left(\widetilde{\nabla}\mathbf{F}\right)_c^* \mathbf{U}_{40} = -\mathbf{q}_{01} \\ &\left(\widetilde{\nabla}\mathbf{F}\right)_c^* \mathbf{U}_{41} = -\mathbf{q}_{02} \\ &\left(4k_c^2\mathbf{D} - \widetilde{\nabla}\mathbf{F}\right)_c^* \mathbf{U}_{42} = \mathbf{q}_{21} + 4k_c\sigma\mathbf{\Lambda}\hat{\mathbf{U}}_{22} \\ &\left(4k_c^2\mathbf{D} - \widetilde{\nabla}\mathbf{F}\right)_c^* \mathbf{U}_{43} = \mathbf{q}_{22} - 4k_c L\mathbf{\Lambda}\hat{\mathbf{U}}_{22} \\ &\left(16k_c^2\mathbf{D} - \widetilde{\nabla}\mathbf{F}\right)_c^* \mathbf{U}_{44} = \mathbf{q}_4 \\ &\hat{\mathbf{U}}_{42} = 2k_c\mathbf{D}\mathbf{U}_{42} - 2\sigma\mathbf{\Lambda}\hat{\mathbf{U}}_{22} \\ &\hat{\mathbf{U}}_{43} = 2k_c\mathbf{D}\,\mathbf{U}_{43} + 2L\mathbf{\Lambda}\hat{\mathbf{U}}_{22} \\ &\hat{\mathbf{U}}_{44} = 4k_c\mathbf{D}\,\mathbf{U}_{44} \end{aligned} \tag{A.7}$$

with

$$\begin{aligned} \mathbf{q}_{01} =& \frac{1}{2}\left[\left(\mathbf{r}\cdot\widetilde{\nabla}\right)\left(\left(\mathbf{U}_{31}\cdot\widetilde{\nabla}\right)\mathbf{F}\right)\right]_c^* - 2\sigma\mathbf{U}_{20} + B_2\left[\left(\mathbf{U}_{20}\cdot\widetilde{\nabla}\right)\frac{d\mathbf{F}}{dB}\right]_c^* + \frac{B_2}{4}\left[\left(\mathbf{r}\cdot\widetilde{\nabla}\right)^{(2)}\frac{d\mathbf{F}}{dB}\right]_c^* \\ \mathbf{q}_{02} =& \frac{1}{2}\left[\left(\mathbf{r}\cdot\widetilde{\nabla}\right)\left(\left(\mathbf{U}_{32}\cdot\widetilde{\nabla}\right)\mathbf{F}\right)\right]_c^* + \frac{1}{4}\left[\left(\mathbf{r}\cdot\widetilde{\nabla}\right)^{(2)}\left(\left(\mathbf{U}_{20}\cdot\widetilde{\nabla}\right)\mathbf{F}\right)\right]_c^* + \\ &+ \frac{1}{8}\left[\left(\mathbf{r}\cdot\widetilde{\nabla}\right)^{(2)}\left(\left(\mathbf{U}_{22}\cdot\widetilde{\nabla}\right)\mathbf{F}\right)\right]_c^* + \frac{1}{4}\left(\left(\mathbf{U}_{22}\cdot\widetilde{\nabla}\right)^{(2)}\mathbf{F}\right)_c^* + \\ &+ \frac{1}{2}\left[\left(\mathbf{U}_{20}\cdot\widetilde{\nabla}\right)^{(2)}\mathbf{F}\right]_c^* + \frac{1}{64}\left[\left(\mathbf{r}\cdot\widetilde{\nabla}\right)^{(4)}\mathbf{F}\right]_c^* + 2L\mathbf{U}_{20} \\ \mathbf{q}_{21} =& \frac{1}{2}\left[\left(\mathbf{r}\cdot\widetilde{\nabla}\right)\left(\left(\mathbf{U}_{31}\cdot\widetilde{\nabla}\right)\mathbf{F}\right)\right]_c^* + B_2\left[\left(\mathbf{U}_{22}\cdot\widetilde{\nabla}\right)\frac{d\mathbf{F}}{dB}\right]_c^* + \frac{B_2}{4}\left[\left(\mathbf{r}\cdot\widetilde{\nabla}\right)^{(2)}\frac{d\mathbf{F}}{dB}\right]_c^* - 2\sigma\mathbf{U}_{22} \\ \mathbf{q}_{22} =& \frac{1}{2}\left[\left(\mathbf{r}\cdot\widetilde{\nabla}\right)\left(\left(\mathbf{U}_{32}\cdot\widetilde{\nabla}\right)\mathbf{F}\right)\right]_c^* + \frac{1}{4}\left[\left(\mathbf{r}\cdot\widetilde{\nabla}\right)^{(2)}\left(\left(\mathbf{U}_{20}\cdot\widetilde{\nabla}\right)\mathbf{F}\right)\right]_c^* + \\ &+ \frac{1}{4}\left[\left(\mathbf{r}\cdot\widetilde{\nabla}\right)^{(2)}\left(\left(\mathbf{U}_{22}\cdot\widetilde{\nabla}\right)\mathbf{F}\right)\right]_c^* + \frac{1}{2}\left[\left(\mathbf{r}\cdot\widetilde{\nabla}\right)\left(\left(\mathbf{U}_{33}\cdot\widetilde{\nabla}\right)\mathbf{F}\right)\right]_c^* + \\ &+ \left[\left(\mathbf{U}_{20}\cdot\widetilde{\nabla}\right)\left(\left(\mathbf{U}_{22}\cdot\widetilde{\nabla}\right)\mathbf{F}\right)\right]_c^* + \frac{1}{48}\left[\left(\mathbf{r}\cdot\widetilde{\nabla}\right)^{(4)}\mathbf{F}\right]_c^* + 2L\mathbf{U}_{22} \\ \mathbf{q}_4 =& \frac{1}{2}\left[\left(\mathbf{r}\cdot\widetilde{\nabla}\right)\left(\left(\mathbf{U}_{33}\cdot\widetilde{\nabla}\right)\mathbf{F}\right)\right]_c^* + \frac{1}{4}\left[\left(\left(\mathbf{U}_{22}\cdot\widetilde{\nabla}\right)^{(2)}\mathbf{F}\right)\right]_c^* + \\ &+ \frac{1}{8}\left[\left(\mathbf{r}\cdot\widetilde{\nabla}\right)^{(2)}\left(\left(\mathbf{U}_{22}\cdot\widetilde{\nabla}\right)\mathbf{F}\right)\right]_c^* + \frac{1}{192}\left[\left(\mathbf{r}\cdot\widetilde{\nabla}\right)^{(4)}\mathbf{F}\right]_c^* \end{aligned} \tag{A.8}$$

Finally, taking into account (22), the elimination of the secular terms at the fifth perturbative order $(15)_5$ leads to the quintic Stuart–Landau equation for the amplitude Ω

$$\frac{\mathbf{d}\Omega}{\mathbf{d}T} = \overline{\sigma}\,\Omega - \overline{L}\,\Omega^3 + \overline{R}\,\Omega^5 \tag{A.9}$$

where

$$\frac{\mathbf{d}}{\mathbf{d}T} = \frac{\partial}{\partial T_2} + \varepsilon^2 \frac{\partial}{\partial T_4}$$
$$\overline{\sigma} = \sigma + \varepsilon^2 \widetilde{\sigma}, \qquad \overline{L} = L + \varepsilon^2 \widetilde{L}, \qquad \overline{R} = \varepsilon^2 \widetilde{R} \tag{A.10}$$

being $\widetilde{\sigma}$, $\widetilde{L}$ and $\widetilde{R}$ the new corrections that arise from higher order terms.

In particular, for the extended Klausmeier model (2)–(4), (33) the coefficients involved in (44)–(46) reduce to

$$\omega_{10} = \frac{B_2\left\{E_1\left[r_1\left(1-\alpha^2u_S^4\right)-\left(2B_c\alpha r_1-r_2\right)\frac{\mathrm{d}u_S^2}{\mathrm{d}B}\right]+r_1^2\left(1+\alpha u_S^2\right)^2\left[2r_1k_c(\beta r_1-r_2)(\tau^u-\tau^w)-r_2Y_1(\tau^uk_c^2+1)\right]\right\}}{4k_c^2r_2Y_1\left(1+\alpha u_S^2\right)^2\left\{r_2+d(\beta r_1-r_2)\left[1-k_c^2(\tau^u-\tau^w)\right]\right\}}$$

$$\omega_{20} = \frac{B_2\left[r_1\left(1-\alpha^2u_S^4\right)-\left(2B_c\alpha r_1-r_2\right)\frac{\mathrm{d}u_S^2}{\mathrm{d}B}\right]\left\{r_1E_1-2k_cr_2Y_1^2\left[r_1+r_2-k_c^2\left(dr_2\tau^w+r_1\tau^u-d\beta r_1\tau^w\right)\right]\right\}}{4k_c^2r_1^2Y_1\left(1+\alpha u_S^2\right)^2\left\{r_2+d(\beta r_1-r_2)\left[1-k_c^2(\tau^u-\tau^w)\right]\right\}}+$$
$$+\frac{B_2\left\{r_1\left[2r_1k_c(\beta r_1-r_2)(\tau^u-\tau^w)-r_2Y_1(\tau^uk_c^2+1)\right]+2k_cr_2Y_1^2(\tau^uk_c^2-1)\right\}}{4k_c^2Y_1\left\{r_2+d(\beta r_1-r_2)\left[1-k_c^2(\tau^u-\tau^w)\right]\right\}}$$

$$\omega_{30} = \frac{B_2\left\{\left[r_1\left(1-\alpha^2u_S^4\right)-\left(2B_c\alpha r_1-r_2\right)\frac{\mathrm{d}u_S^2}{\mathrm{d}B}\right]\left[E_1+4k_c^2r_2Y_1\tau^u(r_1+dr_2-d\beta r_1)\right]+r_1^2\left(1+\alpha u_S^2\right)^2\left[2r_1k_c(\beta r_1-r_2)(\tau^u-\tau^w)+r_2Y_1(3k_c^2\tau^u-1)\right]\right\}}{4k_cr_2Y_1\left(1+\alpha u_S^2\right)^2\left\{r_2+d(\beta r_1-r_2)\left[1-k_c^2(\tau^u-\tau^w)\right]\right\}}$$

$$\omega_{40} = \frac{-dB_2\left(r_1+r_2\frac{\mathrm{d}u_S^2}{\mathrm{d}B}\right)\left\{r_1(\beta r_1-r_2)\left[E_1+4k_c^2r_1Y_1\tau^w(r_1+dr_2-\beta dr_1)\right]+2k_cr_2^2Y_1^2\left[r_1+r_2-k_c^2\left(r_1\tau^u+dr_2\tau^w-d\beta r_1\tau^w\right)\right]\right\}}{4k_cr_1^2r_2Y_1\left\{r_2+d(\beta r_1-r_2)\left[1-k_c^2(\tau^u-\tau^w)\right]\right\}}+$$
$$-\frac{dB_2\left\{2r_1^2k_c(\beta r_1-r_2)^2(\tau^u-\tau^w)-r_1r_2(\beta r_1-r_2)Y_1\left[1+k_c^2(\tau^u-4\tau^w)\right]-2k_cr_2^2Y_1^2(k_c^2\tau^u-1)\right\}}{4k_cr_2Y_1\left\{r_2+d(\beta r_1-r_2)\left[1-k_c^2(\tau^u-\tau^w)\right]\right\}}$$

$$\omega_{11} = \frac{(p_1+8q_1+4s_1)E_1}{32k_c^2r_2Y_1\left\{r_2+d(\beta r_1-r_2)\left[1-k_c^2(\tau^u-\tau^w)\right]\right\}}$$

$$\omega_{21} = \frac{(p_1+8q_1+4s_1)\left\{r_1E_1-2k_cr_2Y_1^2\left[r_1+r_2-k_c^2(\tau^ur_1+d\tau^wr_2-\beta dr_1\tau^w)\right]\right\}}{32k_c^2r_1^2Y_1\left\{r_2+d(\beta r_1-r_2)\left[1-k_c^2(\tau^u-\tau^w)\right]\right\}}$$

$$\omega_{31} = \frac{(p_1+8q_1+4s_1)\left[E_1+4k_c^2r_2Y_1\tau^u(r_1+dr_2-d\beta r_1)\right]}{32Y_1k_cr_2\left\{r_2+d(\beta r_1-r_2)\left[1-k_c^2(\tau^u-\tau^w)\right]\right\}}$$

$$\omega_{41} = \frac{-d(p_1+8q_1+4s_1)\left\{r_1(\beta r_1-r_2)\left[E_1+4k_c^2r_1Y_1\tau^w(r_1+dr_2-\beta dr_1)\right]+2k_cr_2^2Y_1^2\left[r_1+r_2-k_c^2\left(r_1\tau^u+dr_2\tau^w-d\beta r_1\tau^w\right)\right]\right\}}{32k_cr_1^2Y_1\left\{r_2+d(\beta r_1-r_2)\left[1-k_c^2(\tau^u-\tau^w)\right]\right\}}$$

$$\omega_{13} = -\frac{(p_1+12s_1)\left[dr_2(r_1-4Y_1k_c)+r_1^2(1-d\beta)\right]}{768dk_c^3r_2Y_1}$$

$$\omega_{23} = -\frac{(p_1+12s_1)\left[r_1+dr_2+4Y_1k_c-d\beta(4Y_1k_c+r_1)\right]}{768dk_c^3Y_1}$$

$$\eta_{10} = -\frac{E_2\left[2r_1(r_1+dr_2)+d\left(k_cr_2Y_1-2\beta r_1^2\right)\right]+8L\left[2r_1(dn_1r_2-n_2r_1-\beta dn_1r_1)+dk_cn_1r_2Y_1\right]}{4dk_c^3r_2Y_1}$$

$$\eta_{12} = -\frac{E_3\left[2r_1(r_1+dr_2)-d\left(3k_cr_2Y_1+2\beta r_1^2\right)\right]+4L\left[2r_1^2(2k_cm_4\tau^w-m_2+2dk_c\beta m_3\tau^u)+dr_2(m_1-2k_cm_3)(2r_1-3k_cY_1)\right]}{18dk_c^3r_2Y_1}$$

$$\eta_{20} = -\frac{E_2\left[2(r_1+dr_2)-k_cY_1+d\beta(k_cY_1-2r_1)\right]+8L\left[2(dn_1r_2-n_2r_1-\beta dn_2r_1)+k_cY_1(n_2+\beta dn_1)\right]}{4dk_c^3Y_1}$$

$$\eta_{22} = -\frac{E_3\left[2r_1(r_1+dr_2)+3k_cY_1-d\beta(k_cY_1+2r_1)\right]+4L\left[(2k_cm_4\tau^w-m_2+2d\beta k_cm_3\tau^u-d\beta m_1)(2r_1+3k_cY_1)+2dr_2(\gamma_0m_1-2k_cm_3\tau^u)\right]}{18dk_c^3Y_1}$$

$$\zeta_{10} = -\frac{\left[2r_1(r_1+dr_2)+dk_cr_2Y_1-2d\beta r_1^2\right]\left\{B_2S_1+2\left[\left(\omega_{10}r_2+\omega_{20}r_1\right)\left(1+\alpha u_{S_C}^2\right)u_{S_C}+\omega_{10}r_1\left(1-3\alpha u_{S_C}^2\right)w_{S_C}\right]\right\}}{2dk_c^3r_2Y_1\left(1+\alpha u_{S_C}^2\right)^3}+$$
$$-\frac{2n_1r_1^2B_2+2\sigma\left[2r_1(r_1n_2-dr_2n_1)-dk_cn_1r_2Y_1+2d\beta r_1^2n_1\right]}{dk_c^3r_2Y_1}$$

$$\zeta_{12} = -\frac{\left[2r_1(r_1+dr_2)-3dk_cr_2Y_1-2d\beta r_1^2\right]\left[B_2S_2+2\left[\left(\omega_{10}r_2+\omega_{20}r_1\right)\left(1+\alpha u_{S_C}^2\right)u_{S_C}+\omega_{10}r_1\left(1-3\alpha u_{S_C}^2\right)w_{S_C}\right]\right]}{18dk_c^3r_2Y_1\left(1+\alpha u_{S_C}^2\right)^3}+$$
$$-\frac{2\left\{m_1r_1^2B_2+\sigma\left[2r_1^2(m_2-2k_cm_4\tau^w+\beta dm_1-2\beta dm_3k_c\tau^u)+dr_2(m_1-2k_cm_3\tau^u)(3k_cY_1-2r_1)\right]\right\}}{9dk_c^3r_2Y_1}$$

$$\zeta_{20} = -\frac{\left[2(r_1+dr_2)-k_cY_1-2d\beta(k_cY_1-2r_1)\right]\left\{B_2S_1+2\left[\left(\omega_{10}r_2+\omega_{20}r_1\right)\left(1+\alpha u_{S_C}^2\right)u_{S_C}+\omega_{10}r_1\left(1-3\alpha u_{S_C}^2\right)w_{S_C}\right]\right\}}{2dk_c^3Y_1\left(1+\alpha u_{S_C}^2\right)^3}+$$
$$-\frac{B_2n_1(2r_1-k_cY_1)+2\sigma\left[2(r_1n_2-dr_2n_1)-k_cY_1n_2+d\beta n_1(2r_1-k_cY_1)\right]}{dk_c^3r_2Y_1}$$

$$\zeta_{22} = -\frac{\left[2(r_1+dr_2)+3k_cY_1+d\beta(k_cY_1-2r_1)\right]\left\{B_2S_2+2\left[\left(\omega_{10}r_2+\omega_{20}r_1\right)\left(1+\alpha u_{S_C}^2\right)u_{S_C}+\omega_{10}r_1\left(1-3\alpha u_{S_C}^2\right)w_{S_C}\right]\right\}}{18dk_c^3Y_1\left(1+\alpha u_{S_C}^2\right)^3}+$$
$$-\frac{\left[B_2m_1+2\sigma(m_2-2k_cm_4\tau^w+\beta dm_1-2\beta dm_3k_c\tau^u)\right](3k_cY_1+2r_1)-4\sigma r_2(m_1-2k_cm_3\tau^u)}{9dk_c^3Y_1} \tag{A.11}$$

where

$$
\begin{aligned}
Y_1 &= \frac{2k_c r_1\left(1+\alpha u_{S_c}^2\right)}{k_c^2\left(1+\alpha u_{S_c}^2\right)-B_c\left(1-\alpha u_{S_c}^2\right)}\\
S_1 &= r_1^2\frac{\mathrm{d}w_S}{\mathrm{d}B}+2r_1r_2\frac{\mathrm{d}u_S}{\mathrm{d}B}+2n_2\frac{\mathrm{d}u_S^2}{\mathrm{d}B}+2n_1\\
S_2 &= r_1^2\frac{\mathrm{d}w_S}{\mathrm{d}B}+2r_1r_2\frac{\mathrm{d}u_S}{\mathrm{d}B}+2m_2\frac{\mathrm{d}u_S^2}{\mathrm{d}B}+2m_1\\
E_1 &= 2k_c r_1\left(\beta r_1-r_2\right)\left(\tau^u-\tau^w\right)\left(r_1+dr_2-\beta r_1 d\right)-r_2Y_1\left[r_1+r_2+\tau^u k_c^2\left(r_1+dr_2\right)+\right.\\
&\quad \left.+dk_c^2r_2\left(\tau^u-\tau^w\right)-\beta r_1 dk_c^2\left(2\tau^u-\tau^w\right)\right]\\
E_2 &= \frac{1}{\left(1+\alpha u_{S_C}^2\right)^3}\left\{\left[r_1^2\left(m_2+2n_2\right)+2r_1r_2\left(m_1+2n_1\right)+4r_1\omega_{11}w_{S_C}+2w_{S_C}\left(m_1^2+2n_1^2\right)\right]\left(1-3\alpha u_{S_C}^2\right)+\right.\\
&\quad \left.+4\left(m_1m_2+2n_1n_2+r_1\omega_{21}+r_2\omega_{11}\right)\left(1+\alpha u_{S_C}^2\right)u_{S_C}\right\}+\\
&\quad +\frac{3\alpha r_1^2}{2\left(1+\alpha u_{S_C}^2\right)^5}\left\{r_1^2\left(10\alpha u_{S_C}^2-5\alpha^2u_{S_C}^4-1\right)w_{S_C}+4u_{S_C}\left(\alpha^2u_{S_C}^4-1\right)\left[r_1r_2+2\left(m_1+2n_1\right)w_S\right]\right\}\\
E_3 &= \frac{1}{\left(1+\alpha u_{S_C}^2\right)^3}\left\{\left[r_1^2\left(m_2+n_2\right)+2r_1r_2\left(m_1+n_1\right)+2r_1\left(\omega_{11}+\omega_{13}\right)w_{S_C}+4m_1n_1w_{S_C}\right]\left(1-3\alpha u_{S_C}^2\right)\right.\\
&\quad \left.+2\left[r_1\left(\omega_{21}+\omega_{23}\right)+r_2\left(\omega_{11}+\omega_{13}\right)+2\left(m_1n_2+m_2n_1\right)\right]\left(1+\alpha u_{S_C}^2\right)u_{S_C}\right\}+\\
&\quad +\frac{\alpha r_1^2}{\left(1+\alpha u_{S_C}^2\right)^5}\left\{r_1\left(10\alpha u_{S_C}^2-5\alpha^2u_{S_C}^4-1\right)w_{S_C}+4\left[r_1r_2+3\left(m_1+n_1\right)w_{S_C}\right]\left(\alpha^2u_{S_C}^4-1\right)u_{S_C}\right\}
\end{aligned}
\tag{A.12}
$$

Moreover, taking into account systems (21), the second order coefficient appearing in (A.11)–(A.12) reduce to

$$
\begin{aligned}
n_1 &= \frac{r_1^2\left(2k_c^2-B_c\right)}{2u_{S_c}B_c\left[\left(1+\alpha\right)u_{S_c}^2-1\right]}, & n_2 &= -B_cn_1,\\
m_1 &= \frac{1+4dk_c^2}{9}n_1, & m_2 &= -\frac{\left[B_c+4k_c^2\left(1-d\beta\right)\right]}{9}n_1,\\
m_3 &= 2k_cm_1, & m_4 &= 2dk_c\left(m_2-\beta m_1\right).
\end{aligned}
\tag{A.13}
$$

References

[1] Rietkerk M, Bastiaansen R, Banerjee S, Van De Koppel J, Baudena M, Doelman A. Evasion of tipping in complex systems through spatial pattern formation. Science 2021;374. http://dx.doi.org/10.1126/science.abj0359.

[2] Meron E. Nonlinear physics of ecosystems. 1st ed.. Boca Raton: CRC Press; 2015, http://dx.doi.org/10.1201/b18360.

[3] Klausmeier CA. Regular and irregular patterns in semiarid vegetation. Science 1999;284(5421):1826–8. http://dx.doi.org/10.1126/science.284.5421.1826.

[4] Prevedello J, Gotelli N, Metzger J. A stochastic model for landscape patterns of biodiversity. Ecol Monograph 2016;86:462–79. http://dx.doi.org/10.1002/ecm.1223.

[5] Dixon S, Huntly N, Greenwood P, L. Gordillo. A stochastic model for water-vegetation systems and the effect of decreasing precipitation on semi-arid environments. Math Biosci Eng 2018;15:1155–64. http://dx.doi.org/10.3934/mbe.2018052.

[6] Martinez-Garcia R, Cabal C, Calabrese JM, Hernández-García E, Tarnita CE, López C, Bonachela JA. Integrating theory and experiments to link local mechanisms and ecosystem-level consequences of vegetation patterns in drylands. Chaos Solitons Fractals 2023;166:112881. http://dx.doi.org/10.1016/j.chaos.2022.112881.

[7] Rietkerk M, Boerlijst MC, van Langevelde F, HilleRisLambers R, van de Koppel J, Prins HHT, et al. Self-organisation of vegetation in arid ecosystems. Amer Nat 2002;160(4):534. http://dx.doi.org/10.1086/342078.

[8] HilleRisLambers R, Rietkerk M, van de Bosch F, Prins HHT, de Kroon H. Vegetation pattern formation in semi-arid grazing systems. Ecology 2001;82(1):50. http://dx.doi.org/10.1890/0012-9658(2001)082[0050:VPFISA]2.0.CO;2.

[9] Meron E, Gilad E, Von Hardenberg J, Shachak M, Zarmi Y. Vegetation patterns along a rainfall gradient. Chaos Solitons Fractals 2004;19:367–76. http://dx.doi.org/10.1016/S0960-0779(03)00049-3.

[10] Sherratt JA. An analysis of vegetation stripe formation in semi-arid landscapes. J Math Biol 2005;51:183–97. http://dx.doi.org/10.1007/s00285-005-0319-5.

[11] Thompson S, Katul G, McMahon SM. Role of biomass spread in vegetation pattern formation within arid ecosystems. Water Resour Res 2008;44(10):W10421. http://dx.doi.org/10.1029/2008WR006916.

[12] Saco PM, Willgoose GR, Hancock GR. Eco-geomorphology of banded vegetation patterns in arid and semi-arid regions. Hydrol Earth Syst Sci 2007;11:1717–30. http://dx.doi.org/10.1029/2008GL036044.

[13] Borgogno F, D'Odorico P, Laio F, Ridolfi L. Mathematical models of vegetation pattern formation in ecohydrology. Rev Geophisics 2009;47(1):RG1005. http://dx.doi.org/10.1029/2007RG000256.

[14] Ursino N, Rulli MC. Combined effect of fire and water scarcity on vegetation patterns in arid lands. Ecol Model 2010;221(19):2353–62. http://dx.doi.org/10.1016/j.ecolmodel.2010.06.018.

[15] Sherratt JA, Synodinos AD. Vegetation patterns and desertification waves in semi-arid environments: mathematical models based on local facilitation in plants. Discrete Cont Dyn Syst Ser B 2012;17(8):2815–27. http://dx.doi.org/10.3934/dcdsb.2012.17.2815.

[16] Sherratt JA. Pattern solutions of the Klausmeier model for banded vegetation in semi-arid environments III: The transition between homoclinic solutions. Physica D 2013;242(1):30–41. http://dx.doi.org/10.1016/j.physd.2012.08.014.

[17] van der Stelt S, Doelman A, Hek G, Rademacher JDM. Rise and fall of periodic patterns for a generalized Klausmeier-Gray-Scott model. J Nonlinear Sci 2013;23(7):39–95. http://dx.doi.org/10.1007/s00332-012-9139-0.

[18] Thompson S, Assouline S, Chen L, Trahktenbrot A, Svoray T, Katul G. Secondary dispersal driven by overland flow in drylands: Review and mechanistic model development. Mov Ecol 2014;2:7. http://dx.doi.org/10.1186/2051-3933-2-7.

[19] Siteur K, Siero E, Eppinga MB, Rademacher JDM, Doelman A, Rietkerk M. Beyond Turing: The response of patterned ecosystems to environmental change. Ecol Complex 2014;20:81–96. http://dx.doi.org/10.1016/j.ecocom.2014.09.002.

[20] Marasco A, Iuorio A, Cartení F, Bonanomi G, Tartakovsky DM, Mazzoleni S, et al. Vegetation pattern formation due to interactions between water availability and toxicity in plant-soil feedback. Bull Math Biol 2014;76(11):2866–83. http://dx.doi.org/10.1007/s11538-014-0036-6.

[21] Siero E, Doelman A, Eppinga MB, Radenacher JDM, Rietkerk M, Siteur K. Striped pattern selection by advective reaction–diffusion systems: Resilience of banded vegetation on slopes. Chaos 2015;25:036411. http://dx.doi.org/10.1063/1.4914450.

[22] Eigentler L, Sherratt JA. An integrodifference model for vegetation patterns in semi-arid environments with seasonality. J Math Biol 2020;81:875–904. http://dx.doi.org/10.1007/s00285-020-01530-w.

[23] Marasco A, Giannino F, Iuorio A. Modelling competitive interactions and plant–soil feedback in vegetation dynamics. Ricerche Mat 2020;69:553—577. http://dx.doi.org/10.1007/s11587-020-00497-6.

[24] Consolo G, Grifó G. Turing vegetation patterns in flat arid environments with finite soil carrying capacity. Ricerche Mat 2023. http://dx.doi.org/10.1007/s11587-023-00783-z.

[25] Consolo G, Valenti G. Secondary seed dispersal in the Klausmeier model of vegetation for sloped semi-arid environments. Ecol Model 2019;402:66–75. http://dx.doi.org/10.1016/j.ecolmodel.2019.02.009.

[26] von Hardenberg J, Meron E, Shachak M, Zarmi Y. Diversity of vegetation patterns and desertification. Phys Rev Lett 2001;87:198101. http://dx.doi.org/10.1103/PhysRevLett.87.198101.

[27] Ghorai S, Poria S. Turing patterns induced by cross-diffusion in a predator-prey system in presence of habitat complexity. Chaos Solitons Fractals 2016;91:421–9. http://dx.doi.org/10.1016/j.chaos.2016.07.003.

[28] Ritchie JS, Krauseb AL, Van Gordera RA. Turing and wave instabilities in hyperbolic reaction-diffusion systems: The role of second-order time derivatives and cross-diffusion terms on pattern formation. Ann Phys 2022;444:169033. http://dx.doi.org/10.1016/j.aop.2022.169033.

[29] Wang F, Yang R. Spatial pattern formation driven by the cross-diffusion in a predator–prey model with Holling type functional response. Chaos Solitons Franctals 2023;174:113890. http://dx.doi.org/10.1016/j.chaos.2023.113890.

[30] Wang X, Zhang G. Vegetation pattern formation in seminal systems due to internal competition reaction between plants. J Theoret Biol 2018;458:10–4. http://dx.doi.org/10.1016/j.jtbi.2018.08.043.

[31] Djilali S, Bentout S, Ghanbari B, Kumar S. Spatial patterns in a vegetation model with internal competition and feedback regulation. Eur Phys J Plus 2021;136:256. http://dx.doi.org/10.1140/epjp/s13360-021-01251-z.

[32] Milchunas DG, Lauenroth WK. Inertia in plant community structure: State changes after cessation of nutrient-enrichment stress. Ecol Appl 1995;5(2):452–8. http://dx.doi.org/10.2307/1942035.

[33] Garcia-Fayos P, Gasque M. Consequences of a severe drought on spatial patterns of woody plants in a two-phase mosaic steppe of Stipa tenacissima L.. J Arid Environ 2002;52(2):199–208. http://dx.doi.org/10.1006/jare.2002.0987.

[34] Deblauwe V, Couteron P, Lejeune O, Bogaert J, Barbier N. Environmental modulation of self-organized periodic vegetation patterns in sudan. Ecography 2011;34(6):990–1001. http://dx.doi.org/10.1111/j.1600-0587.2010.06694.x.

[35] Valentin C, d'Herbes JM. Niger tiger bush as a natural water harvesting system. Catena 1999;37(1–2):231–56. http://dx.doi.org/10.1016/S0341-8162(98)00061-7.

[36] Deblauwe V, Couteron P, Bogaert J, Barbier N. Determinants and dynamics of banded vegetation pattern migration in arid climates. Ecol Monogr 2012;82(1):3–21. http://dx.doi.org/10.1890/11-0362.1.

[37] Barbera E, Curró C, Valenti G. On discontinuous travelling wave solutions for a class of hyperbolic reaction-diffusion models. Physica D 2015;308:116–26. http://dx.doi.org/10.1016/j.physd.2015.06.011.

[38] Consolo G, Curró C, Valenti G. Pattern formation and modulation in a hyperbolic vegetation model for semiarid environments. Appl Math Model 2017;43(3):372–92. http://dx.doi.org/10.1016/j.apm.2016.11.031.

[39] Consolo G, Curró C, Valenti G. Supercritical and subcritical Turing pattern formation in a hyperbolic vegetation model for flat arid environments. Physica D 2019;398(11):141–63. http://dx.doi.org/10.1016/j.physd.2019.03.006.

[40] Consolo G, Curró C, Valenti G. Turing vegetation patterns in a generalized hyperbolic Klausmeier model. Math Methods Appl Sci 2020;43(18):10474. http://dx.doi.org/10.1002/mma.6518.

[41] Consolo G, Curró C, Grifó G, Valenti G. Oscillatory periodic pattern dynamics in hyperbolic reaction-advection-diffusion models. Phys Rev E 2022;105:034206. http://dx.doi.org/10.1103/PhysRevE.105.034206.

[42] Consolo G, Grifó G. Eckhaus instability of stationary patterns in hyperbolic reaction-diffusion models on large finite domains. Partial Differential Equ Appl 2022;3:57. http://dx.doi.org/10.1007/s42985-022-00193-0.

[43] Consolo G, Grifó G, Valenti G. Dryland vegetation pattern dynamics driven by inertial effects and secondary seed dispersal. Ecol Model 2022;474:110171. http://dx.doi.org/10.1016/j.ecolmodel.2022.110171.

[44] Grifó G. Vegetation patterns in the hyperbolic Klausmeier model with secondary seed dispersal. Mathematics 2023;11:1084. http://dx.doi.org/10.3390/math11051084.

[45] Grifó G, Consolo G, Curró C, Valenti G. Rhombic and hexagonal pattern formation in 2D hyperbolic reaction-transport systems in the context of dryland ecology. Physica D 2023;449:133745. http://dx.doi.org/10.1016/j.physd.2023.133745.

[46] Ruggeri T, Sugiyama M. Classical and relativistic rational extended thermodynamics of gases. 1st ed.. Cham: Springer; 2021, http://dx.doi.org/10.1007/978-3-030-59144-1.

[47] Kealy BJ, Wollkind DJ. A nonlinear stability analysis of vegetative Turing pattern formation for an interaction-diffusion plant-surface water model system in an arid flat environment. Bull Math Biol 2012;74(4):803–33. http://dx.doi.org/10.1007/s11538-011-9688-7.

[48] Zelnik Y, Kinast S, Yizhaq H, Bel G, Meron E. Regime shifts in models of dryland vegetation. Phil Trans R Soc A 2013;371(2004):20120358. http://dx.doi.org/10.1098/rsta.2012.0358.

[49] Sun GQ, Li L, Zhang ZK. Spatial dynamics of a vegetation model in an arid flat environment. Nonlinear Dynam 2013;73(5):2207–19. http://dx.doi.org/10.1007/s11071-013-0935-3.

[50] Liu QX, Jin Z, B.L. Li. Numerical investigation of spatial pattern in a vegetation model with feedback function. J Theoret Biol 2008;254:350–60. http://dx.doi.org/10.1016/j.jtbi.2008.05.017.

[51] Shi J, Xie Z, Little K. Cross-diffusion induced instability and stability in reaction-diffusion systems. J Appl Anal Comput 2010;24:95–119. http://dx.doi.org/10.11948/2011007.

[52] Gowda K, Riecke H, Silber M. Transitions between patterned states in vegetation models for semi-arid ecosystems. Phys Rev E 2014;89:022701. http://dx.doi.org/10.1103/PhysRevE.89.022701.

[53] Chaiya I, Wollkind DJ, Cangelosi RA, Kealy-Dichone BJ, Rattanakul C. Vegetative rhombic pattern formation driven by root suction for an interaction–diffusion plant–ground water model system in an arid flat environment. Am J Plant Sci 2015;6:1278–300. http://dx.doi.org/10.4236/ajps.2015.68129.

[54] Sun GQ, Wang CH, Chang LL, Wu YP, Li L. Effects of feedback regulation on vegetation patterns in semi-arid environments. Appl Math Model 2018;61:200–15. http://dx.doi.org/10.1016/j.apm.2018.04.010.

[55] Liu C, Li L, Wang Z, Wang R. Pattern transitions in a vegetation system with cross-diffusion. Appl Math Comput 2019;342:255–62. http://dx.doi.org/10.1016/j.amc.2018.09.039.

[56] Xu S, Zhang C. Spatiotemporal patterns induced by cross-diffusion on vegetation model. AIMS Math 2022;7:14076–5098. http://dx.doi.org/10.3934/math.2022776.

[57] Curró C, Valenti G. Pattern formation in hyperbolic models with cross-diffusion: Theory and applications. Physica D 2021;418(4):132846. http://dx.doi.org/10.1016/j.physd.2021.132846.

[58] Ghorai S, Bairagi N. Instabilities in hyperbolic reaction–diffusion system with cross diffusion and species-dependent inertia. Chaos Solitons Fractals 2022;165:112800. http://dx.doi.org/10.1016/j.chaos.2022.112800.

[59] Sherratt JA. Pattern solutions of the Klausmeier model for banded vegetation in semi-arid environments I. Nonlinearity 2010;23(8):2657–75. http://dx.doi.org/10.1088/0951-7715/23/10/016.

[60] Matlab. Ver 2022b, Natick, Massachusetts: The MathWorks Inc.. 2023, URL https://www.mathworks.com/.

[61] Ermentrout B. Simulating, analyzing, and animating dynamical systems. 1st ed.. Philadelphia: SIAM; 2002, http://dx.doi.org/10.1137/1.9780898718195.

[62] Curró C, Valenti G. Subcritical Turing patterns in hyperbolic models with cross–diffusion. Ricerche Mat 2021;71:147–67. http://dx.doi.org/10.1007/s11587-021-00574-4.